Transcription regulation of SARS-CoV-2 receptor ACE2 by Sp1: a potential therapeutic target

Hui Han[1, 4], Rong-Hua Luo[2, 4], Xin-Yan Long[2, 4], Li-Qiong Wang[3, 4], Qian Zhu[1], Xin-Yue Tang[1], Rui Zhu[1], Yi-Cheng Ma[1, *], Yong-Tang Zheng[2,*], & Cheng-Gang Zou[1,*]

[1]State key Laboratory for Conservation and Utilization of Bio-Resources in Yunnan, School of Life Sciences, Yunnan University, Kunming, Yunnan, 650091, China.

[2]Key Laboratory of Animal Models and Human Disease Mechanisms of the Chinese Academy of Sciences/Key Laboratory of Bioactive Peptides of Yunnan Province, KIZ-CUHK Joint Laboratory of Bio-Resources and Molecular Research in Common Diseases, Kunming Institute of Zoology, Chinese Academy of Sciences, Kunming, Yunnan, 650223, China.

[3]Department of Phathology, Yan'an Hospital, Kunming Medical University, Kunming, Yunnan, 650051, China.

[4]These authors contributed equally

[*]Correspondence: mayc@ynu.edu.cn(Y. M.), zhengyt@mail.kiz.ac.cn(Y.Z.), chgzou@ynu.edu.cn(C.Z.)

Abstract

Angiotensin-converting enzyme 2 (ACE2) is a major cell entry receptor for severe acute respiratory syndrome coronavirus 2 (SARS-CoV-2). Induction of ACE2 expression may represent an effective tactic employed by SARS-CoV-2 to facilitate its own propagation. However, the regulatory mechanisms of ACE2 expression after viral infection remain largely unknown. By employing an array of 45 different luciferase reporters, we identify that the transcription factor Sp1 positively and HNF4α negatively regulate the expression of ACE2 at the transcriptional levels in HPAEpiC cells, a human lung epithelial cell line. SARS-CoV-2 infection promotes and inhibits the transcription activity of Sp1 and HNF4α, respectively. The PI3K/AKT signaling pathway, which is activated by SARS-CoV-2 infection, is a crucial node for induction of ACE2 expression by increasing Sp1 phosphorylation, an indicator of its activity, and reducing HNF4α nuclear location. Furthermore, we show that colchicine could inhibit the PI3K/AKT signaling pathway, thereby suppressing ACE2 expression. Inhibition of Sp1 by either its inhibitor mithramycin A or colchicine reduces viral replication and tissue injury in Syrian hamsters infected with SARS-CoV-2. In summary, our study uncovers a novel function of Sp1 in regulating ACE2 expression and suggests that Sp1 is a potential target to reduce SARS-CoV-2 infection.

Keywords: SARS-CoV-2; ACE2; Sp1; HNF4α; mithramycin A

Introduction

Severe acute respiratory syndrome coronavirus 2 (SARS-CoV-2) is the causative pathogen of coronavirus disease 2019 (COVID-19) (Wu et al., 2020), which has spread rapidly across the world and caused a global public health event (Lu et al., 2020). The pathophysiological features of severe patients with COVID-19 are characterized by systemic inflammatory response, which manifests as acute respiratory distress syndrome and multiorgan dysfunction (Pan et al., 2021, van Eijk et al., 2021). SARS-CoV-2 cell entry depends on the SARS-CoV-2 receptor, angiotensin-converting enzyme 2 (ACE2), and the transmembrane serine protease, TMPRSS2 (Yan et al., 2020). During SARS-CoV-2 infection, the spike protein binds with ACE2 and undergoes cleavage by TMPRSS2 to allow the viral to fuse with host cell membrane, which is essential for viral entry (Hoffmann et al., 2020). ACE2 is wildly expressed in the lung, small intestine, kidney, liver, testis, heart and brain (Dong et al., 2020, Verdecchia et al., 2020). The expression of ACE2 in a wide variety of human tissues may explain why SARS-CoV-2 targets multiple organs.

Vaccination has been proven to be a highly effective way to prevent SARS-CoV-2 infection and reduce the incidence of hospitalization and death. However, due to the continuous mutation of the SARS-CoV-2, a number of individuals cannot mount an adequate immune response to COVID-19 through vaccination alone. The effectiveness of the different types of existing vaccines against the Omicron variants has been greatly reduced (Kuhlmann et al., 2022, Wilhelm et al., 2022). The spike protein of these SARS-CoV-2 variants shows an increased binding affinity to ACE2, leading to enhanced transmission ability (Liu et al., 2021, McCallum et al., 2022). Therefore, it is urgently needed to discover and develop a novel host-directed

therapeutic against SARS-CoV-2, especially in aged population.

Accumulating evident indicates that SARS-CoV-2 infection significantly upregulates ACE2 expression (Gao et al., 2022, Wei et al., 2021, Xu et al., 2021a, Zhuang et al., 2020). SARS-CoV-2 infection upregulates the expression of HMGB1, which in turn induces ACE2 expression probably through an epigenetic mechanism (Wei et al., 2021). Furthermore, overexpression of SARS-CoV-2 spike protein significantly elicits ACE2 expression, which is dependent on the type I interferon signaling (Zhou et al., 2021). Indeed, ACE2 has been proved to be an interferon-stimulated gene (Ziegler et al., 2020). Meanwhile, two recent studies have demonstrated that androgen receptor positively regulates the expression of ACE2 at a transcriptional levels (Qiao et al., 2021, Samuel et al., 2020). Importantly, targeting the transcriptional regulation of ACE2 by reducing AR signaling, through androgen receptor antagonists or degraders attenuate SARS-CoV-2 infectivity (Qiao et al., 2021). A very recent study has demonstrated that ursodeoxycholic acid (UDCA), an inhibitor of the farnesoid X receptor (FXR), reduces ACE2 expression in human lung, intestinal, and liver organoids, thereby inhibiting SARS-CoV-2 infection (Brevini et al., 2022). Thus, ACE2 is a promising therapeutic target in the fight against COVID-19. However, the molecular mechanism underlying SARS-CoV-2 infection-induced ACE2 expression remains largely unknown.

To clarify the molecular mechanism underlying regulation of ACE2 by SARS-CoV-2 and colchicine, we employed a commercial array of 45 different luciferase reporters to assay a range of signaling pathways. Our data revealed that SARS-CoV-2 up-regulated ACE2 expression by activating the transcription factor Sp1 and inhibiting HNF4α through the PI3K/AKT pathway. Finally, we showed that inhibition of Sp1 by its inhibitor mithramycin A was active against

89 SARS-CoV-2 in human respiratory epithelial cells and animal model. Thus, our findings
90 suggest that Sp1 is an important transcription factor for ACE2 expression.
91
92 **Results**
93 **SARS-CoV-2 infection up-regulates ACE2 expression, which is inhibited by colchicine**
94 **treatment**
95 As the receptor for the SARS-CoV-2 viral entry, ACE2 is regarded as a promising therapeutic
96 target in the fight against COVID-19 (Monteil et al., 2020). Consistent with previous
97 observations that SARS-CoV-2 infection significantly upregulates the mRNA expression of
98 ACE2 (Gao et al., 2022, Wei et al., 2021, Xu et al., 2021a, Zhuang et al., 2020), we found that
99 infection by SARS-CoV-2 upregulated the protein levels of ACE2 in HPAEpiC cells, a human
100 lung epithelial cell line (Figure 1A and 1B). Similar results were obtained from
101 immunofluorescence analysis (Figure 1C and 1D). Recent clinical studies have shown a
102 mortality benefit with colchicine, a drug used for the treatment of acute gout and familial
103 Mediterranean fever (Dasgeb et al., 2018, Gasparyan et al., 2015, Schlesinger et al., 2020,
104 Slobodnick et al., 2015), when used in the treatment of COVID-19 patients (Drosos et al., 2022,
105 Elshafei et al., 2021). In this study, we found that treatment with colchicine substantially
106 inhibited ACE2 expression in HPAEpiC cells with or without SARS-CoV-2 infection (Figure
107 1A-D).
108 As colchicine could inhibit ACE2 expression, we assessed the in vitro inhibitory effect of
109 colchicine on SARS-CoV-2 replication in HPAEpiC cells. After preincubated with colchicine
110 at different concentrations for 1 h, cells were infected with SARS-CoV-2 for 1 h and then

111 cultured in fresh medium for 24 h to measure viral RNA copy numbers by quantitative reverse
112 transcriptase PCR (qPCR). We found that colchicine treatment reduced extracellular SARS-
113 CoV-2 replication in cells (Figure 1-figure supplement 1A). The half-maximal effective
114 concentration (EC_{50}) value of colchicine for inhibiting viral replication was 0.2703 μM (Figure
115 1-figure supplement 1B). These data suggest that inhibition of ACE2 expression by colchicine
116 suppresses SARS-CoV-2 infection.
117
118 **SARS-CoV-2 infection regulates the transcription activity of Sp1 and HNF4α**
119 To clarify the molecular mechanism for the regulation of ACE2 expression, we used colchicine,
120 as proof-of-principle. We analyzed a range of signaling pathways in response to SARS-CoV-2
121 infection in the presence or absence of colchicine using cignal finder 45-pathway reporter array
122 (Manzini et al., 2014, Xu et al., 2021b) (Figure 2A). Of all the signaling pathways tested, there
123 were three transcription factors (Sp1, NF-κB, and GATA) enhanced by SARS-CoV-2 infection,
124 and suppressed by colchicine (Figure 2A). Meanwhile, there were two signaling pathways
125 (HNF4α and estrogen receptor) inactivated by SARS-CoV-2 infection and activated by
126 colchicine treatment (Figure 2A). Thus, these transcription factors are potential candidates for
127 regulating ACE2 expression. We thus analyzed the DNA motifs in 1.5 kb upstream of the
128 transcription start sites (TSS) of ACE2 gene using the MEME program (Bailey et al., 2015).
129 Our data revealed two significantly enriched motifs (Figure 2B), which were annotated as the
130 motif of transcription factors including Sp1 (P = 6.1e-5), HNF4α (P = 4.2e-5). These results
131 implicate that these two transcription factors are likely involved in regulating ACE2 expression.
132 To determine the effects of SARS-CoV-2 and colchicine on the activities of Sp1 and

HNF4α, the subcellular distribution of Sp1 and HNF4α were detected using immunofluorescence. Although Sp1 was mainly located in nucleus of HPAEpiC cells (Figure 2-figure supplement 1), only a small portion of total Sp1 was phosphorylated at Thr453 (Figure 2C), which is an indicator of its activation (Milanini-Mongiat et al., 2002). SARS-CoV-2 infection remarkably increased the levels of phospho-Sp1 (Thr453), whereas colchicine treatment significantly inhibited the phosphorylation of Sp1 in the presence or absence of SARS-CoV-2 (Figure 2C and 2D). Unlike Sp1, HNF4α exhibited a dual nuclear and cytoplasmic distribution in HPAEpiC cells under basal conditions (Figure 2E). Whereas SARS-CoV-2 infection induced a nuclear to cytoplasmic shift in the distribution of HNF4α, supplementation with colchicine induced nuclear accumulation of HNF4α in the presence or absence of SARS-CoV-2 (Figure 2E and 2F). These results suggest that SARS-CoV-2 infection results in activation of Sp1 and inactivation of HNF4α, which is reversed by colchicine treatment.

Sp1 and HNF4α is involved in ACE2 expression

Next, we investigated whether colchicine inhibited ACE2 expression by regulation of Sp1 and HNF4α. First, western blot analysis demonstrated that like colchicine, either treatment with a selective Sp1 inhibitor mithramycin A (MithA) or knockdown of Sp1 by siRNA downregulated the protein levels of ACE2 in HPAEpiC cells (Figure 3A and 3B). However, inhibition of Sp1 by MithA or siSp1 did not further reduce the protein expression of ACE2 downregulated by colchicine. In contrast, both treatment with an HNF4α antagonist BI6015 and knockdown of HNF4α by siRNA upregulated the protein levels of ACE2 (Figure 3C and 3D). Furthermore,

155 colchicine blocked this increase in the protein expression of ACE2 induced by BI6015 or
156 siHNF4α.

157 Second, immunofluorescence staining of ACE2 revealed that although MithA treatment
158 inhibited the protein expression of ACE2, it did not further reduce the protein expression of
159 ACE2 suppressed by colchicine (Figure 3E and 3F). Supplementation with BI6015 markedly
160 increased the expression of ACE2 in HPAEpiC cells, which was reduced by treated with
161 colchicine (Figure 3E and 3F). Similar results were obtained in A549 cells, a human lung
162 epithelial cell line (Figure 3-figure supplement 1).

163 Third, using a luciferase reporter gene containing the ACE2 promoter, we observed that
164 supplementation with MithA treatment inhibit the luciferase activity, but did not reduce the
165 luciferase activity in the presence of colchicine (Figure 3G). In contrast, treatment with BI6015
166 increased the luciferase activity. In addition, chromatin immunoprecipitation (ChIP)–qPCR
167 analysis demonstrated that the binding of Sp1 to the GC box of ACE2 promoter was
168 significantly reduced, whereas the binding of HNF4α to the AGGTCA element was markedly
169 increased after colchicine treatment (Figure 3H). As MithA is capable of inhibiting the
170 expression of ACE2, we tested whether this compound could inhibit SARS-CoV-2 infection in
171 vitro. Our results demonstrated that MithA inhibited SARS-CoV-2 replication with EC50 of
172 0.1948 μM in HPAEpiC cells (Figure 3-figure supplement 2). Taken together, these results
173 suggest that Sp1 and HNF4α act in an opposite way on the regulation of ACE2 expression at
174 the transcription level to affect the susceptibility of cells to SARS-CoV-2 infection.

175

176 **Sp1 and HNF4α antagonized each other**

Interestingly, we found that treatment with the Sp1 inhibitor MithA significantly suppressed the phosphorylation of Sp1, whereas treatment with the HNF4α antagonist BI6015 led to an increase in the levels of phospho-Sp1 (Thr453) (Figure 4A and 4B). Conversely, BI6015 treatment induced cytoplasmic translocation of HNF4α, whereas MithA treatment promoted nuclear accumulation of HNF4α (Figure 4C and 4D). Likewise, western blotting analysis revealed that the phosphorylation level of Sp1 was increased after knockdown of HNF4α by siRNA (Figure 4E and 4F). By contrast, knockdown of Sp1 did not affect the levels of total HNF4α. These data led us to test whether Sp1 could interact with HNF4α. Co-immunoprecipitation assay (co-IP) confirmed the interaction between Sp1 and HNF4α in HPAEpiC cells (Figure 4G). These data indicate that Sp1 and HNF4α antagonize each other probably by protein-protein interaction.

Colchicine reduces ACE2 expression by inhibiting the PI3K/AKT signaling pathway

It has been reported that the PI3K/AKT signaling pathway is activated by SARS-CoV-2 infection (Callahan et al., 2021, Sun et al., 2021, Klann et al., 2020). Consistent with these observations, we found that SARS-CoV-2 infection enhanced phosphorylation of AKT at Ser473 and Thr308, which is required for its activation (Su et al., 2011) (Figure 5A-5C). However, colchicine treatment substantially inhibited SARS-CoV-2-induced AKT phosphorylation (Figure 5A-5C). Furthermore, either knockdown of AKT by siRNA or treatment with two PI3K/AKT inhibitors (LY294002 and wortmannin) downregulated the expression of ACE2 in HPAEpiC cells (Figure 5D-5G). Finally, we found that LY294002 and wortmannin inhibited SARS-CoV-2 infection in HPAEpiC cells, with EC_{50} of 0.2381 μM and

199 0.04228 μM, respectively (Figure 5-figure supplement 1). These data suggest that the
200 PI3K/AKT signaling pathway is required for SARS-CoV-2 infection.

201 The PI3K/AKT signaling pathway plays an important role in regulating the transcriptional
202 activity of Sp1 and HNF4α (Adapala et al., 2019, Gomez-Villafuertes et al., 2015, Zhao et al.,
203 2015, Li et al., 2019). Activation of AKT promotes the stability and localization of Sp1 by
204 phosphorylating Sp1 at threonine sites 453 and 739 (Adapala et al., 2019, Gomez-Villafuertes
205 et al., 2015, Zhao et al., 2015), and prevents the nuclear translocation of HNF4α (Li et al., 2019).
206 Consistent with these observations, we found that suppression of AKT by siRNA or its
207 inhibitors significantly inhibited the accumulation of phospho-Sp1 in the nucleus, but
208 remarkably promoted nuclear translocation of HNF4α (Figure 5H-5K). Taken together, these
209 data indicate that inhibition of the PI3K/AKT signaling pathway is required for downregulation
210 of ACE2 expression mediated by colchicine via regulation of Sp1 and HNF4α transcription
211 activities.

212

213 **Inhibition of Sp1 reduces the viral load and damage to the respiratory and renal systems**

214 Finally, we tested whether inhibition of Sp1 by colchicine and MithA could inhibit the
215 replication of SARS-CoV-2 in vivo by using Syrian hamsters (*Mesocricetus auratus*), an animal
216 model used for the study of COVID-19 pneumonia and the evaluation of therapeutics (Chan et
217 al., 2020, Choudhary et al., 2022, Muñoz-Fontela et al., 2020, Rosenke et al., 2021, Sia et al.,
218 2020). Two groups of hamsters were intranasally infected with SARS-CoV-2 at a dose of 10^4
219 $TCID_{50}$ (Tissue culture infective dose). One hour later, hamsters were inoculated
220 intraperitoneally with colchicine or MithA at 0.2 mg/kg, respectively. A mock group was treated

with vehicle using the same route and timing (Figure 6-figure supplement 1). These animals were dosed every 24 h with either colchicine or MithA at 0.2 mg/kg, respectively. Lung and trachea samples were collected at 3 days post-infection for assessing viral RNA and ACE2 expression. Immunofluorescence analysis demonstrated that the expression of ACE2 was significantly upregulated in the lung and trachea of hamsters infected with SARS-CoV-2, compared to that of animals without infection (control group) (Figure 6A and 6B; Figure 6-figure supplement 2A and Figure 6-figure supplement 2B). However, treatment with colchicine or MithA substantially inhibited the expression of ACE2 in both of the lung and trachea of hamsters infected with SARS-CoV-2. Based on immunofluorescence analysis for SARS-CoV-2 nucleocapsid and qPCR, we found that treatment with colchicine or MithA reduced viral replication in both of the lung and trachea of hamsters (Figure 6C-6F; Figure Figure 6-figure supplement 2C and Figure 6-figure supplement 2D), respectively.

Next, histopathological analysis of the lung tissue on day 3 post-infection showed pulmonary lesions consisting of necrosis and nuclear pyknosis in bronchial epithelial cells, massive hemorrhage in the alveolar space, a significant invasion of inflammatory cells, and edema (Figure 6G and 6I). In addition, alveolar walls were significantly thickened. While the treatment groups had similar lesions, they were much less severe than the mock group. Using Masson's trichrome staining, we observed collagen deposition, a hallmark of fibrosis, in the lung of infected hamsters (Figure 6H and 6J). However, treatment with colchicine or MithA effectively reversed lung fibrosis. Taken together, these results suggest that colchicine and MithA antagonize SARS-CoV-2 replication in the lung and trachea, and attenuate histopathological damage in the lung.

Although severe SARS-CoV-2-associated acute kidney injury serves as an independent risk factor for in-hospital death in patients (Nadim et al., 2020), whether SARS-CoV-2 can directly infect the kidney remains unclear (Wysocki et al., 2021, Smith and Akilesh, 2021). The prevailing evidence seems to favor indirect means of kidney injury in SARS-CoV-2 (Smith and Akilesh, 2021). Based on immunofluorescence analysis, the presence of massive SARS-CoV-2 was observed in the kidney of infected hamsters, which was slightly reduced by treatment with colchicine or MithA (Figure 7A and 7B). Immunofluorescence analysis showed that treatment with the two drugs could effectively reduce the expression of ACE2 (Figure 7C and 7D). Histopathological analysis indicated a significant damage in the kidney of hamsters infected with SARS-CoV-2, including renal tubular epithelial cell nuclear pyknosis, brush border disappearance; renal interstitial vascular congestion, inflammatory cell infiltration; glomerular atrophy (Figure 7E and 7F). By contrast, the glomeruli were evenly distributed, and the structure was intact; the tubular epithelial cells were normal, and the brush borders were neatly arranged in these drug-treated animals. There was no obvious abnormality in the medulla, and no obvious hyperplasia of the renal interstitium. Taken together, treatment with colchicine and MithA leads to a significant improvement in renal histology.

Discussion

Based on our study and our current understanding of SARS-CoV-2 infection, we propose a model for how SARS-CoV-2 infection induces ACE2 expression through a mechanism involving two transcription factors, Sp1 and HNF4α, in host cells. Under normal conditions, Sp1 is mainly located in nucleus, whereas HNF4α exhibit a dual nuclear and cytoplasmic

distribution in cells. The two transcription factors regulate ACE2 expression in an opposite manner, leading to a basal expression of ACE2. After SARS-CoV-2 infection, the PI3K/AKT signaling pathway is activated (Klann et al., 2020). This signaling pathway in turn promotes the transcription activity of Sp1 by increasing its phosphorylation in nucleus, and suppresses the transcription activity of HNF4α by inducing its cytoplasmic translocation. A disruption of this balance leads to the upregulation of ACE2. Since ACE2 is the receptor for the SARS-CoV-2 viral entry, induction of ACE2 expression may represent an effective tactic employed by the virus to facilitate its own propagation.

Multi-omics approaches have recently been applied to understand host responses to SARS-CoV-2, thus accelerating drug development and drug repositioning against COVID-19 (Kamel et al., 2021, Lu et al., 2022, Chu et al., 2021, Ho et al., 2021, Klann et al., 2020). For instance, phosphoproteomic analysis of SARS-CoV-2-infected cells has revealed the activation of growth factor receptor (GFR) and its downstream pathways including the RAF/MEK/ERK MAPK signaling and PI3K/AKT/mTOR signaling in SARS-CoV-2-infected cells (Klann et al., 2020). Inhibition of the GFR signaling by using prominent anti-cancer drugs, such assorafenib (the RAF inhibitor), RO5126766 (the dual RAF/MEK inhibitor), and pictilisib (the PI3K inhibitor), and omipalisib (the dual PI3K and mTOR inhibitor), prevents SARS-CoV-2 replication in cells. By screening a panel of 45 signaling pathways in SARS-CoV-2-infected HPAEpiC cells in the presence or absence of colchicine, we showed that two transcription factors Sp1 and HNF4α are involved in regulation of ACE2 expression in an opposite manner. Sp1 positively and HNF4α negatively regulate the expression of ACE2 at the transcriptional levels. The PI3K/AKT signaling pathway, which is activated by SARS-CoV-2 infection (Klann

et al., 2020), is a crucial node for induction of ACE2 expression by promoting the transcriptional activity of Sp1 and reducing the transcriptional activity of HNF4α.

Our data indicate that down-regulation of ACE2 expression by inhibiting Sp1 activity attenuates SARS-CoV-2 replication in the lung and trachea of Syrian hamsters. Importantly, this inhibition of viral replication in these tissues is associated with markedly reduced lung pathology. Acute kidney injury is another extrapulmonary manifestation of severe COVID-19 (Legrand et al., 2021). However, a direct causal association between SARS-CoV-2 infection and the development of acute kidney injury has been controversial (Legrand et al., 2021, Smith and Akilesh, 2021). Recently, Jansen et al. have demonstrated that SARS-CoV-2 directly infects kidney cells by using human-induced pluripotent stem cell-derived kidney organoids (Jansen et al., 2022). Our data show that colchicine treatment effectively suppresses the expression of ACE2 in the proximal tubule of kidney, which is accompanied by reduced SARS-CoV-2-induced kidney injury in Syrian hamsters. Our results support the notion that ACE2 is a promising therapeutic target in the fight against COVID-19 (Monteil et al., 2020). For example, proxalutamide, a potent androgen receptor antagonist, can suppress the expression of ACE2, which is induced by androgens through androgen receptor (Qiao et al., 2021). Moreover, inhibition of RIPK1 reduces viral load in cultured human lung organoids infected by SARS-CoV-2, which is accompanied by downregulating the transcriptional induction of ACE2 (Xu et al., 2021a). Very recently, Brevini et al. reveal that FXR is involved in the regulation of ACE2 expression in multiple tissues. Inhibition of FXR activity by UDCA downregulates ACE2 expression and reduces SARS-CoV-2 infection in vitro, in vivo and ex vivo (Brevini et al., 2022).

While studying the effect of Sp1 and HNF4α inhibitors on ACE2 expression, we unexpectedly observed that inhibition of Sp1 by its inhibitor MithA induces nuclear accumulation of HNF4α, whereas inhibition of HNF4α by its antagonist BI6015 increases the phosphorylation levels of Sp1 in nucleus. How do the two transcription factors antagonize each other? Although the action of MithA is to interfere with Sp1 binding to its consensus site (Lee et al., 2011), the Sp1 inhibitor is capable of inducing proteasome-dependent Sp1 degradation (Lee et al., 2012, Choi et al., 2014). This may explain why MithA treatment significantly suppresses the phosphorylation levels of Sp1 in our experiments. Likewise, BI6015 can suppress HNF4α expression, although the function of the HNF4α antagonist is to repress HNF4α DNA binding (Kiselyuk et al., 2012). This again provides a ready explanation of our observation that BI6015 could inhibit nuclear accumulation of HNF4α induced by colchicine. More importantly, our results demonstrate that non-phosphorylated Sp1, but not phosphorylated Sp1, can interact with HNF4α. On the basis of these results, one may speculate that the interaction between HNF4α and Sp1 may block Sp1 phosphorylation. Reduced protein levels of HNF4α by BI6015 leads to release of more Sp1, which is ready for phosphorylation by AKT. Phosphorylated Sp1 then binds to the GC box and upregulates ACE2 expression. On the other hand, a decrease in Sp1 protein levels by MithA leads to release of more HNF4α. This transcription factor in turn inhibits ACE2 expression by binding to the HNF4α-specific binding motif. These data may help us to further understand how Sp1 and HNF4α antagonize each other's transcription activity. Clearly, the underlying mechanisms need to be further investigated in light of our current results.

Increased expression of ACE2 in the airway and lung contributes to the severity of

COVID-19 symptoms in elderly patients (Inde et al., 2021). At present, the newly emerging SARS-CoV-2 Omicron variants have become the dominant strain worldwide. The Omicron spike protein has six-fold to nine-fold increased affinity for binding to ACE2 (Yin et al., 2022). Various types of available vaccines, which are based on the original strain of SARS-CoV-2, are ineffective against Omicron variants (Wilhelm et al., 2022, Kuhlmann et al., 2022). Our findings may contribute to knowledge for developing a new host-targeting approach for the fight against COVID-19, especially for the elderly patients with SARS-CoV-2 Omicron variant infection.

Material and Methods

Cell culture

Immortalized human alveolar epithelial cells (HPAEpiCs) were generated from human lung tissue type II pneumocytes (purchased from the ScienCell Research Laboratory (San Diego, CA)) and maintained in RPMI 1640 medium (01-100-1ACS, Biological Industries, Israel) supplemented with 10 % fetal bovine serum (FBS) (C04001-050X10, VivaCell, Shanghai, China), and 1 % penicillin-streptomycin. A549 cells were maintained in DMEM/F12 medium (C3130-0500, VivaCell) containing 10 % FBS, and 1 % penicillin-streptomycin. All cells were cultured in 5 % CO2, 95 % air incubator at 37 °C.

HPAEpiCs and A549 cells were treated with colchicine (C804812, Macklin, Shanghai, China), mithramycin A (MithA, A600668, Sangon Biotech, Shanghai, China), BI6015 (HY-108469, Med Chem Express, Shanghai, China), LY294002 (HY-10108, Med Chem Express), or wortmannin (HY-10197, Med Chem Express). DMSO was used as a control. Cells were

353 infected with SARS-CoV-2 at MOI of 1 for 1 h.

354

355 **SARS-CoV-2**

356 The SARS-CoV-2 strain (accession number: NMDCN0000HUI) was provided by the
357 Guangdong Provincial Center for Disease Control and Prevention (Guangzhou, China). The
358 virus was propagated in African green monkey kidney epithelial cells (Vero-E6) (ATCC, No.
359 1586) and titrated. All the infection experiments were performed in a biosafety level-3 (BLS-3)
360 laboratory.

361

362 **Half-maximal effect concentration (EC_{50})**

363 HPAEpiC cells were seeded at a density of 1.6×10^4 cell/well in 48-well plates and grown
364 overnight. Cells were then infected with SARS-CoV-2 at MOI of 1. At the same time, the test
365 compounds were added to the wells with different concentrations. After 1 h of incubation at
366 37 °C, the virus-drug mixture was removed and washed 3 times to remove free virus with PBS,
367 replaced with fresh medium containing compounds. After 48 h, the supernatants were collected
368 to extract viral RNA for RT-qPCR analysis. The EC_{50} values were calculated by using a dose-
369 response model in GraphPad Prism 8.0 software (GraphPad Software Inc., La Jolla, CA).

370

371 **Cellular antiviral activity assay**

372 HPAEpiC cells were seeded at a density of 4×10^5 cell/well in 24-well plates and grown
373 overnight. After preincubated with the test compounds for 2 h, the cells were infected with
374 SARS-CoV-2 at an MOI of 1. After 1 h of incubation at 37 °C, the virus-drug mixtures were

375 replaced with fresh medium containing compounds. In 24 h, cells were collected to extract total
376 RNA and total cell protein. Viral RNA was quantified by THUNDERBIRD Probe One-step RT-
377 qPCR Kit (QRZ-101, Toyobo, Shanghai, China). TaqMan primers for SARS-CoV-2 are 5'-
378 GGG GAA CTT CTC CTG CTA GAA T-3' and 5'-CAG ACA TTT TGC TCT CAA GCT G-3'
379 with SARS-CoV-2 probe FAM-TTG CTG CTG CTT GAC AGA TT-TAMRA-3'.
380
381 **Quantitative real-time PCR**
382 The total RNA was extracted from Trachea and lung tissues using the RNAiso Plus (Takara,
383 Dalian, China). Total RNA was extracted from cells with TRIzol™ Reagent (R1100, Solarbio,
384 Shanghai, China), and reverse-transcribed into cDNA using FastKing RT Kit (KR116,
385 TIANGEN, Beijing, China). qPCR analysis was performed using SuperReal PreMix Plus
386 (SYBR Green) (FP205, TIANGEN) on a Roche LightCycler 480 System (Roche Applied
387 Science, Mannheim, Germany). Primers used for qPCR were followed: ACE2 (Forward 5'-
388 GGG ATC AGA GAT CGG AAG AAG AAA-3'; Reverse 5'-AGG AGG TCT GAA CAT CAT
389 CAG TG-3'); ACTB (Forward 5'-CCC TGG ACT TCG AGC AAG AG-3'; Reverse 5'-ACT
390 CCA TGC CCA GGA AGG AA-3'). The relative mRNA expression levels of ACE2 were
391 assessed by the $2^{-\Delta\Delta Ct}$ method. ACTB was used to calculate relative expression normalized to
392 an internal control.
393
394 **45-Pathway Reporter Array**
395 Cignal Finder 45-Pathway Reporter Arrays (CCA-901, Qiagen, Hilden, Germany) were used
396 according to the manufacturer's instructions to identify potential pathways regulated by SARS-

CoV-2. Briefly, HPAEpiC cells were reverse transfected with firefly luciferase reporter constructs containing response elements for the indicated pathways, and control Renilla luciferase constructs for 24 h. Cells were then pretreated with colchicine for 2 h and incubated with SARS-CoV-2 for 24 h. Then, the luciferase activities of the cells were measured with a dual-luciferase reporter assay system (E1910, Promega) on a fluorescent microplate reader (Molecular Devices Inc). Reporter luciferase activity was normalized to Renilla luciferase activity for each sample. All experiments were performed with three biological replicates.

Immunofluorescence

Cells were fixed with 4% paraformaldehyde (PFA) for 10 min at room temperature. Paraformaldehyde-fixed, paraffin-embedded tissue was cut into 4 μm and adhered to frosted glass slides. After washed with PBS and treated with PBS containing 0.1% Triton X-100 for 15 min, the sections or cells were then permeabilized and blocked with PBST containing 5% fetal bovine serum for 90 min at room temperature. Cells were immunostained with anti-ACE2 (ab15348, 1:500 dilution, Abcam), or anti-Sp1 (T453) (ab59257, 1:500 dilution, Abcam), or anti-HNF4α antibodies (3113, 1:1000 dilution, Cell Signaling Technology) overnight at 4 °C. Tissue sections were immunostained with anti-ACE2 (GB11267, 1:200**,** Servicebio, Wuhan, China) or anti-SARS-CoV-2-N antibodies (40143-MM05, 1:500 dilution, SinoBiological, Beijing, China) overnight at 4°C. After washed three times with 0.1% Tween-20 in PBS (PBST), these cells were incubated with Alexa Fluor 594 anti-Rabbit IgG (H+L) (A-21207, 1:200 dilution, ThermoFisher Scientific), or Cy3 conjugated Goat anti-mouse IgG (H+L) (GB21301, 1:300**,** Servicebio), or Alexa Fluor 488-conjugated Goat anti-Rabbit IgG (H+L) (GB25303,

1:500**,** Servicebio) for 1 h. After staining with primary antibodies, nuclei were counterstained with DAPI. Images were acquired using a Zeiss Axioskop 2 plus fluorescence microscope (Carl Zeiss, Jena, Germany).

Luciferase reporter assay

HPAEpiC cells at a density of 3×10^3 were co-transfected with pRL-SV40 vector and phACE2-promoter-TA-luc (D2488, Beyotime) using Lipofectamine 3000 reagent (L3000015, Invitrogen). After 48 h of transfection, the luciferase activity was measured using the dual-luciferase reporter assay system (E1910, Promega, Shanghai, China) on a fluorescent microplate reader (Molecular Devices Inc., Sunnyvale, CA). The ratio of firefly luciferase to Renilla luciferase was calculated for each experiment and averaged from 3 replicates. All experiments were performed with three biological replicates.

Transcription factor binding motif enrichment analysis

The ACE2 promoter sequence (1500 bp upstream of the transcription start site) was extracted from the NCBI database. The DNA-binding motifs of transcription factors ER, GATA6, HNF4α, NF-κB, and Sp1 were obtained from the JASPAR CORE database (JASPAR-A database of transcription factor binding profiles (genereg.net)). Then, the MEME Suite (Introduction-MEME Suite (meme-suite.org)) was used to interrogate the enrichment of these transcription factor motifs and the binding sites in the ACE2 promoter sequence (Bailey et al., 2015). FIMO analysis was performed using stringent criteria including *P*-value < 1E-4 and a maximum of two mismatched residues.

441

442 **ChIP-qPCR**

443 ChIP was performed as described previously (Tao et al., 2016). Briefly, chromatin
444 immunoprecipitation (ChIP) assay was performed using the ChIP assay kit (P2078, Beyotime)
445 following the manufacturer's directions as described. After crosslinking with formaldehyde, the
446 chromatin solutions were sonicated and incubated with anti-Sp1 (9389, 1:100 dilution, Cell
447 Signaling Technology), anti-HNF4α (ab181604, 1:100 dilution, Abcam) antibodies, and control
448 IgG, and rotated overnight at 4 °C, respectively. After purified by a DNA purification kit
449 (BioTeke Corp.), the immunoprecipitated DNA was detected for PCR analysis. All ChIP-qPCR
450 experiments were performed with three biological replicates.

451

452 **RNA interference for cells**

453 All chemically synthesized siRNAs were obtained from Gene-Pharma Corporation (Shanghai,
454 China). To silence the expression of HNF4α, or Sp1, or AKT by siRNA, HPAEpiC were seeded
455 at density of 5×10^5 cells per well in 6-well plates containing complete culture medium. After
456 24 h, cells were transiently transfected with 100 nM of siRNAs using Lipofectamine 3000
457 (L3000015, Invitrogen, Beijing, China). Gene silencing efficiency was confirmed by qPCR 48
458 h post-transfection. The following siRNAs were used (sequence of the sense strand): HNF4α,
459 5'-GUC AUC GUU GCC AAC ACA AUG-3'; Sp1, 5'-CUC CAA GGC CUG GCU AAU
460 AAU-3'; AKT, 5'-CGC GUG ACC AUG AAC GAG UUU-3'; negative control, 5'-UUC UCC
461 GAA CGU GUC ACG UUU-3'.

462

463 **Co-immunoprecipitation**

464 For co-immunoprecipitation experiments, HPAEpiC cells were lysed on ice for 30 min in cell
465 lysis buffer (P0013, Beyotime, Shanghai, China). After centrifugation at 12000 rpm for 30 min
466 at 4 °C. The supernatant was collected and incubated with anti-HNF4α antibodies (ab181604,
467 1:70 dilution, Abcam, Shanghai, China) overnight. After 4 h incubation with Protein A Agarose
468 (20333, Thermo Scientific, Shanghai, China) at 4 °C, the complexes were washed three times.
469 Immunoblotting was performed after elution.

470

471 **Western blot**

472 For measurement of protein expression, HPAEpiC cells were re-suspended in RIPA buffer
473 (R0278, Sigma-Aldrich, Shanghai, China) on ice for 1 hour. Protein samples were separated on
474 SDS-PAGE gels, and then transferred to polyvinylidene fluoride (PVDF) membranes. After
475 blocking with 5% BSA in PBS-T buffer containing 0.05% Tween-20, the membranes were
476 incubated with primary antibodies overnight at 4 °C. Primary antibodies used in this study
477 included: anti-ACE2 (ab108252, 1:1000 dilution, Abcam), anti-HNF4α (ab181604, 1:1000
478 dilution, Abcam), anti-phospho-AKT (Thr308) (13038, 1:1000 dilution, Cell Signaling
479 Technology, Shanghai, China), anti-phospho-AKT (Ser473) (4060, 1:1000 dilution, Cell
480 Signaling Technology), anti-pan-AKT (4691, 1:1000 dilution, Cell Signaling Technology),
481 anti-phospho-Sp1 (T453) (ab59257, 1:1000 dilution, Abcam), and anti-Actin antibodies (sc-
482 47778, 1:5000 dilution, Santa Cruz-Biotechnology, Shanghai, China). After washed with PBS-
483 T, the membranes were incubated with horseradish peroxidase (HRP)-conjugated secondary
484 antibodies for 2 h at room temperature. The secondary antibodies used in our experiments were

HRP-conjugated anti-mouse (7076, 1:2000 dilution, Cell Signaling Technology) or anti-rabbit IgG antibodies (7074, 1:2000 dilution, Cell Signaling Technology). The protein bands were detected using ECL (RPN2232, GE Healthcare, Little Chalfont, UK) on Amersham Imager 600. Subsequent image analysis was performed using ImageJ software. All experiments were performed with three biological replicates.

Animal experiments and in vivo procedures

Syrian hamsters (*Mesocricetus auratus*) were purchased from Beijing Vital River Laboratory Animal Technology Co., Ltd. weighting 85-100 g, aged 5 weeks, male. In this study, all animals used were chosen randomly. The colchicine (C804812, Macklin, Shanghai, China) and MithA (A600668, Sangon Biotech, Shanghai, China) were dissolved in 1% (v/v) DMSO and 99% saline. The Syrian hamsters were anesthetized by inhalation of isoflurane and infected with 10^4 $TCID_{50}$ of SARS-CoV-2 by intranasal instillation. One hour later, 0.2 mg/kg of either colchicine or MithA were given i.p. once daily. Trachea, lung, and kidney tissues were collected on days 3 post infection.

H&E staining and histopathology score

Lungs, trachea and kidney from Syrian hamsters were collected, and fixed with 4% paraformaldehyde and then paraffin-embedded. Tissue sections at 4 μm thickness were stained with hematoxylin and eosin (H&E) for histopathological examination. After H&E staining, a four-point scoring system was applied to assess the severity of pathology in tissues. The grades are expressed as numbers, where 0 indicates no pathological change and 1-4 indicate increasing

507 severity. Lung histopathological scores were assessed and summarized based on alveolar wall
508 thickening, edema, hemorrhage, and inflammatory cell infiltration. Kidney histopathological
509 scores were assessed and summarized based on cellular degeneration, necrosis, hemorrhage,
510 inflammatory cell infiltration, and congestion. Histopathological scores represent the sum of
511 the injury subtype scores for each condition on a scale of 0-20.
512
513 **Statistical analysis**
514 Differences in gene expression, mRNA and protein levels, Viral RNA, Luciferase reporter assay,
515 ChIP-qPCR assay, and fluorescence intensity were assessed by performing Student's t-test.
516 Data were analyzed using GraphPad Prism 8 (GraphPad Software Inc., La Jolla, CA).
517
518 **Study approval**
519 In this study, all animal experimental procedures were approved by the Institutional Committee
520 for Animal Care and Biosafety at Kunming Institute of Zoology, Chinese Academy of Sciences
521 (Permit Number: IACUC-RE-2021-10-002).
522
523 **Data availability**
524 All data generated or analysed during this study are included in the manuscript and supporting
525 file.
526
527 **Author contributions**
528 C.G. Z., Y.T. Z., Y.C. M., H. H., and R.H. L. designed the experiments and analyzed the data.

H. H., R.H. L., X.Y. L., L.Q. W., Q. Z., X.Y. T., and R. Z. D performed the experiments. C.G. Z., Y.T. Z., Y.C. M., H. H., and R.H. L. interpreted the data. C.G. Z., Y.T. Z., Y.C. M., and H. H. wrote the manuscript.

Acknowledgements

We thank Dr. Changwen Ke (Guangdong Provincial Center for Disease Control and Prevention) for providing SARS-CoV-2 strain. We appreciate all the support from Kunming National High-level Biosafety Research Center for Non-human Primates, Kunming Institute of Zoology, Chinese Academy of Sciences. This work was supported in part by grants from the National Key Research and Development Program of China (2021YFC2301303), Yunnan Key Research and Development Program (202103AC100005, 202103AQ100001, 202102AA310055), and the Major Science and Technology Project in Yunnan Province of China (202001BB050001).

Declaration of interests

Authors declare that they have no competing interests.

References

ADAPALA, N. S., ROOT, S., LORENZO, J., AGUILA, H. & SANJAY, A. 2019. PI3K activation increases SDF-1 production and number of osteoclast precursors, and enhances SDF-1-mediated osteoclast precursor migration. *Bone Reports,* 10**,** 100203.

BAILEY, T. L., JOHNSON, J., GRANT, C. E. & NOBLE, W. S. 2015. The MEME Suite. *Nucleic Acids Research,* 43**,** W39-49.

551 BREVINI, T., MAES, M., WEBB, G. J., JOHN, B. V., FUCHS, C. D., BUESCHER, G., WANG, L.,
552 GRIFFITHS, C., BROWN, M. L., SCOTT, W. E., PEREYRA-GERBER, P., GELSON, W. T.
553 H., BROWN, S., DILLON, S., MURARO, D., SHARP, J., NEARY, M., BOX, H., TATHAM,
554 L., STEWART, J., CURLEY, P., PERTINEZ, H., FORREST, S., MLCOCHOVA, P.,
555 VARANKAR, S. S., DARVISH-DAMAVANDI, M., MULCAHY, V. L., KUC, R. E.,
556 WILLIAMS, T. L., HESLOP, J. A., ROSSETTI, D., TYSOE, O. C., GALANAKIS, V., VILA-
557 GONZALEZ, M., CROZIER, T. W. M., BARGEHR, J., SINHA, S., UPPONI, S. S., FEAR, C.,
558 SWIFT, L., SAEB-PARSY, K., DAVIES, S. E., WESTER, A., HAGSTRöM, H., MELUM, E.,
559 CLEMENTS, D., HUMPHREYS, P., HERRIOTT, J., KIJAK, E., COX, H., BRAMWELL, C.,
560 VALENTIJN, A., ILLINGWORTH, C. J. R., DAHMAN, B., BASTAICH, D. R., FERREIRA,
561 R. D., MARJOT, T., BARNES, E., MOON, A. M., BARRITT, A. S., GUPTA, R. K., BAKER,
562 S., DAVENPORT, A. P., CORBETT, G., GORGOULIS, V. G., BUCZACKI, S. J. A., LEE, J.-
563 H., MATHESON, N. J., TRAUNER, M., FISHER, A. J., GIBBS, P., BUTLER, A. J., WATSON,
564 C. J. E., MELLS, G. F., DOUGAN, G., OWEN, A., LOHSE, A. W., VALLIER, L.,
565 SAMPAZIOTIS, F. & CONSORTIUM, U.-P. R. 2022. FXR inhibition may protect from SARS-
566 CoV-2 infection by reducing ACE2. *Nature*.

567 CALLAHAN, V., HAWKS, S., CRAWFORD, M. A., LEHMAN, C. W., MORRISON, H. A., IVESTER,
568 H. M., AKHRYMUK, I., BOGHDEH, N., FLOR, R., FINKIELSTEIN, C. V., ALLEN, I. C.,
569 WEGER-LUCARELLI, J., DUGGAL, N., HUGHES, M. A. & KEHN-HALL, K. 2021. The
570 Pro-Inflammatory Chemokines CXCL9, CXCL10 and CXCL11 Are Upregulated Following
571 SARS-CoV-2 Infection in an AKT-Dependent Manner. *Viruses,* 13.

572 CHAN, J. F.-W., ZHANG, A. J., YUAN, S., POON, V. K.-M., CHAN, C. C.-S., LEE, A. C.-Y., CHAN,

W.-M., FAN, Z., TSOI, H.-W., WEN, L., LIANG, R., CAO, J., CHEN, Y., TANG, K., LUO, C., CAI, J.-P., KOK, K.-H., CHU, H., CHAN, K.-H., SRIDHAR, S., CHEN, Z., CHEN, H., TO, K. K.-W. & YUEN, K.-Y. 2020. Simulation of the Clinical and Pathological Manifestations of Coronavirus Disease 2019 (COVID-19) in a Golden Syrian Hamster Model: Implications for Disease Pathogenesis and Transmissibility. *Clinical Infectious Diseases,* 71**,** 2428-2446.

CHOI, E.-S., NAM, J.-S., JUNG, J.-Y., CHO, N.-P. & CHO, S.-D. 2014. Modulation of specificity protein 1 by mithramycin A as a novel therapeutic strategy for cervical cancer. *Scientific Reports,* 4**,** 7162.

CHOUDHARY, S., KANEVSKY, I., YILDIZ, S., SELLERS, R. S., SWANSON, K. A., FRANKS, T., RATHNASINGHE, R., MUNOZ-MORENO, R., JANGRA, S., GONZALEZ, O., MEADE, P., COSKRAN, T., QIAN, J., LANZ, T. A., JOHNSON, J. G., TIERNEY, C. A., SMITH, J. D., TOMPKINS, K., ILLENBERGER, A., CORTS, P., CIOLINO, T., DORMITZER, P. R., DICK, E. J., SHIVANNA, V., HALL-URSONE, S., COLE, J., KAUSHAL, D., FONTENOT, J. A., MARTINEZ-ROMERO, C., MCMAHON, M., KRAMMER, F., SCHOTSAERT, M. & GARCíA-SASTRE, A. 2022. Modeling SARS-CoV-2: Comparative Pathology in Rhesus Macaque and Golden Syrian Hamster Models. *Toxicologic Pathology***,** 01926233211072767.

CHU, J., XING, C., DU, Y., DUAN, T., LIU, S., ZHANG, P., CHENG, C., HENLEY, J., LIU, X., QIAN, C., YIN, B., WANG, H. Y. & WANG, R.-F. 2021. Pharmacological inhibition of fatty acid synthesis blocks SARS-CoV-2 replication. *Nature Metabolism,* 3**,** 1466-1475.

DASGEB, B., KORNREICH, D., MCGUINN, K., OKON, L., BROWNELL, I. & SACKETT, D. L. 2018. Colchicine: an ancient drug with novel applications. *British Journal of Dermatology,* 178**,** e167-e167.

595 DONG, M., ZHANG, J., MA, X., TAN, J., CHEN, L., LIU, S., XIN, Y. & ZHUANG, L. 2020. ACE2,
596 TMPRSS2 distribution and extrapulmonary organ injury in patients with COVID-19.
597 *Biomedicine & Pharmacotherapy,* 131**,** 110678.
598 DROSOS, A. A., PELECHAS, E., DROSSOU, V. & VOULGARI, P. V. 2022. Colchicine Against SARS-
599 CoV-2 Infection: What is the Evidence? *Rheumatology and Therapy,* 9**,** 379-389.
600 ELSHAFEI, M. N., EL-BARDISSY, A., KHALIL, A., DANJUMA, M., MUBASHER, M., ABUBEKER,
601 I. Y. & MOHAMED, M. F. H. 2021. Colchicine use might be associated with lower mortality
602 in COVID-19 patients: A meta-analysis. *European Journal of Clinical Investigation,* 51**,** e13645.
603 GAO, C.-C., LI, M., DENG, W., MA, C.-H., CHEN, Y.-S., SUN, Y.-Q., DU, T., LIU, Q.-L., LI, W.-J.,
604 ZHANG, B., SUN, L., LIU, S.-M., LI, F., QI, F., QU, Y., GE, X., LIU, J., WANG, P., NIU, Y.,
605 LIANG, Z., ZHAO, Y.-L., HUANG, B., PENG, X.-Z., YANG, Y., QIN, C., TONG, W.-M. &
606 YANG, Y.-G. 2022. Differential transcriptomic landscapes of multiple organs from SARS-CoV-
607 2 early infected rhesus macaques. *Protein & Cell,* 13**,** 920-939.
608 GASPARYAN, A. Y., AYVAZYAN, L., YESSIRKEPOV, M. & KITAS, G. D. 2015. Colchicine as an
609 anti-inflammatory and cardioprotective agent. *Expert Opinion on Drug Metabolism &*
610 *Toxicology,* 11**,** 1781-1794.
611 GOMEZ-VILLAFUERTES, R., GARCIA-HUERTA, P., DIAZ-HERNANDEZ, J. I. & MIRAS-
612 PORTUGAL, M. T. 2015. PI3K/Akt signaling pathway triggers P2X7 receptor expression as a
613 pro-survival factor of neuroblastoma cells under limiting growth conditions. *Scientific Reports,*
614 5**,** 18417.
615 HO, J. S. Y., MOK, B. W.-Y., CAMPISI, L., JORDAN, T., YILDIZ, S., PARAMESWARAN, S.,
616 WAYMAN, J. A., GAUDREAULT, N. N., MEEKINS, D. A., INDRAN, S. V., MOROZOV, I.,

TRUJILLO, J. D., FSTKCHYAN, Y. S., RATHNASINGHE, R., ZHU, Z., ZHENG, S., ZHAO, N., WHITE, K., RAY-JONES, H., MALYSHEVA, V., THIECKE, M. J., LAU, S.-Y., LIU, H., ZHANG, A. J., LEE, A. C.-Y., LIU, W.-C., JANGRA, S., ESCALERA, A., AYDILLO, T., MELO, B. S., GUCCIONE, E., SEBRA, R., SHUM, E., BAKKER, J., KAUFMAN, D. A., MOREIRA, A. L., CAROSSINO, M., BALASURIYA, U. B. R., BYUN, M., ALBRECHT, R. A., SCHOTSAERT, M., GARCIA-SASTRE, A., CHANDA, S. K., MIRALDI, E. R., JEYASEKHARAN, A. D., TENOEVER, B. R., SPIVAKOV, M., WEIRAUCH, M. T., HEINZ, S., CHEN, H., BENNER, C., RICHT, J. A. & MARAZZI, I. 2021. TOP1 inhibition therapy protects against SARS-CoV-2-induced lethal inflammation. *Cell,* 184**,** 2618-2632.e17.

HOFFMANN, M., KLEINE-WEBER, H., SCHROEDER, S., KRüGER, N., HERRLER, T., ERICHSEN, S., SCHIERGENS, T. S., HERRLER, G., WU, N. H., NITSCHE, A., MüLLER, M. A., DROSTEN, C. & PöHLMANN, S. 2020. SARS-CoV-2 Cell Entry Depends on ACE2 and TMPRSS2 and Is Blocked by a Clinically Proven Protease Inhibitor. *Cell,* 181**,** 271-280.e8.

INDE, Z., CROKER, B., YAPP, C., JOSHI, G. N., SPETZ, J., FRASER, C., QIN, X. P., XU, L., DESKIN, B., GHELFI, E., WEBB, G., CARLIN, A. F., ZHU, Y. F. P. P., LEIBEL, S. L., GARRETSON, A. F., CLARK, A. E., DURAN, J. M., PRETORIUS, V., CROTTY-ALEXANDER, L. E., LI, C. D., LEE, J. C., SODHI, C., HACKAM, D. J., SUN, X., HATA, A. N., KOBZIK, L., MILLER, J., PARK, J. A., BROWNFIELD, D., JIA, H. P. & SAROSIEK, K. A. 2021. Age-dependent regulation of SARS-CoV-2 cell entry genes and cell death programs correlates with COVID-19 severity. *Science Advances,* 7.

JANSEN, J., REIMER, K. C., NAGAI, J. S., VARGHESE, F. S., OVERHEUL, G. J., DE BEER, M., ROVERTS, R., DAVIRAN, D., FERMIN, L. A. S., WILLEMSEN, B., BEUKENBOOM, M.,

DJUDJAJ, S., VON STILLFRIED, S., VAN EIJK, L. E., MASTIK, M., BULTHUIS, M., DUNNEN, W. D., VAN GOOR, H., HILLEBRANDS, J.-L., TRIANA, S. H., ALEXANDROV, T., TIMM, M.-C., VAN DEN BERGE, B. T., VAN DEN BROEK, M., NLANDU, Q., HEIJNERT, J., BINDELS, E. M. J., HOOGENBOEZEM, R. M., MOOREN, F., KUPPE, C., MIESEN, P., GRüNBERG, K., IJZERMANS, T., STEENBERGEN, E. J., CZOGALLA, J., SCHREUDER, M. F., SOMMERDIJK, N., AKIVA, A., BOOR, P., PUELLES, V. G., FLOEGE, J., HUBER, T. B., ACHDOUT, H., AIMON, A., BAR-DAVID, E., BARR, H., BEN-SHMUEL, A., BENNETT, J., BOBY, M. L., BORDEN, B., BOWMAN, G. R., BRUN, J., BVNBS, S., CALMIANO, M., CARBERY, A., CATTERMOLE, E., CHERNYCHENKO, E., CHODER, J. D., CLYDE, A., COFFLAND, J. E., COHEN, G., COLE, J., CONTINI, A., COX, L., CVITKOVIC, M., DIAS, A., DONCKERS, K., DOTSON, D. L., DOUANGAMATH, A., DUBERSTEIN, S., DUDGEON, T., DUNNETT, L., EASTMAN, P. K., EREZ, N., EYERMANN, C. J., FAIRHEAD, M., FATE, G., FEARON, D., FEDEROV, O., FERLA, M., FERNANDES, R. S., FERRINS, L., FOSTER, R., FOSTER, H., GABIZON, R., GARCIA-SASTRE, A., GAWRILJUK, V. O., GEHRTZ, P., GILEADI, C., GIROUD, C., GLASS, W. G., GLEN, R., ITAI, G., GODOY, A. S., GORICHKO, M., GORRIE-STONE, T., GRIFFEN, E. J., HART, S. H., HEER, J., HENRY, M., et al. 2022. SARS-CoV-2 infects the human kidney and drives fibrosis in kidney organoids. *Cell Stem Cell,* 29**,** 217-231.e8.

KAMEL, W., NOERENBERG, M., CERIKAN, B., CHEN, H., JäRVELIN, A. I., KAMMOUN, M., LEE, J. Y., SHUAI, N., GARCIA-MORENO, M., ANDREJEVA, A., DEERY, M. J., JOHNSON, N., NEUFELDT, C. J., CORTESE, M., KNIGHT, M. L., LILLEY, K. S., MARTINEZ, J., DAVIS, I., BARTENSCHLAGER, R., MOHAMMED, S. & CASTELLO, A. 2021. Global analysis of

protein-RNA interactions in SARS-CoV-2-infected cells reveals key regulators of infection. *Molecular Cell,* 81**,** 2851-2867.e7.

KISELYUK, A., LEE, S.-H., FARBER-KATZ, S., ZHANG, M., ATHAVANKAR, S., COHEN, T., PINKERTON, ANTHONY B., YE, M., BUSHWAY, P., RICHARDSON, ADAM D., HOSTETLER, HEATHER A., RODRIGUEZ-LEE, M., HUANG, L., SPANGLER, B., SMITH, L., HIGGINBOTHAM, J., CASHMAN, J., FREEZE, H., ITKIN-ANSARI, P., DAWSON, MARCIA I., SCHROEDER, F., CANG, Y., MERCOLA, M. & LEVINE, F. 2012. HNF4α Antagonists Discovered by a High-Throughput Screen for Modulators of the Human Insulin Promoter. *Chemistry & Biology,* 19**,** 806-818.

KLANN, K., BOJKOVA, D., TASCHER, G., CIESEK, S., MüNCH, C. & CINATL, J. 2020. Growth Factor Receptor Signaling Inhibition Prevents SARS-CoV-2 Replication. *Molecular Cell,* 80**,** 164-174.e4.

KUHLMANN, C., MAYER, C. K., CLAASSEN, M., MAPONGA, T., BURGERS, W. A., KEETON, R., RIOU, C., SUTHERLAND, A. D., SULIMAN, T., SHAW, M. L. & PREISER, W. 2022. Breakthrough infections with SARS-CoV-2 omicron despite mRNA vaccine booster dose. *The Lancet,* 399**,** 625-626.

LEE, K.-A., CHAE, J.-I. & SHIM, J.-H. 2012. Natural diterpenes from coffee, cafestol and kahweol induce apoptosis through regulation of specificity protein 1 expression in human malignant pleural mesothelioma. *Journal of Biomedical Science,* 19**,** 60.

LEE, Y. C., OSLUND, K. L., THAI, P., VELICHKO, S., FUJISAWA, T., DUONG, T., DENISON, M. S. & WU, R. 2011. 2,3,7,8-Tetrachlorodibenzo-p-dioxin–Induced MUC5AC Expression. *American Journal of Respiratory Cell and Molecular Biology,* 45**,** 270-276.

683 LEGRAND, M., BELL, S., FORNI, L., JOANNIDIS, M., KOYNER, J. L., LIU, K. & CANTALUPPI,
684 V. 2021. Pathophysiology of COVID-19-associated acute kidney injury. *Nature Reviews*
685 *Nephrology,* 17**,** 751-764.
686 LI, M., WANG, Y., XIA, X., MO, P., XU, J., YU, C. & LI, W. 2019. Steroid receptor coactivator 3 inhibits
687 hepatitis B virus gene expression through activating Akt signaling to prevent HNF4alpha
688 nuclear translocation. *Cell & Bioscience,* 9**,** 64.
689 LIU, C., GINN, H. M., DEJNIRATTISAI, W., SUPASA, P., WANG, B., TUEKPRAKHON, A.,
690 NUTALAI, R., ZHOU, D., MENTZER, A. J., ZHAO, Y., DUYVESTEYN, H. M. E., LóPEZ-
691 CAMACHO, C., SLON-CAMPOS, J., WALTER, T. S., SKELLY, D., JOHNSON, S. A.,
692 RITTER, T. G., MASON, C., COSTA CLEMENS, S. A., GOMES NAVECA, F.,
693 NASCIMENTO, V., NASCIMENTO, F., FERNANDES DA COSTA, C., RESENDE, P. C.,
694 PAUVOLID-CORREA, A., SIQUEIRA, M. M., DOLD, C., TEMPERTON, N., DONG, T.,
695 POLLARD, A. J., KNIGHT, J. C., CROOK, D., LAMBE, T., CLUTTERBUCK, E., BIBI, S.,
696 FLAXMAN, A., BITTAYE, M., BELIJ-RAMMERSTORFER, S., GILBERT, S. C., MALIK,
697 T., CARROLL, M. W., KLENERMAN, P., BARNES, E., DUNACHIE, S. J., BAILLIE, V.,
698 SERAFIN, N., DITSE, Z., DA SILVA, K., PATERSON, N. G., WILLIAMS, M. A., HALL, D.
699 R., MADHI, S., NUNES, M. C., GOULDER, P., FRY, E. E., MONGKOLSAPAYA, J., REN, J.,
700 STUART, D. I. & SCREATON, G. R. 2021. Reduced neutralization of SARS-CoV-2 B.1.617
701 by vaccine and convalescent serum. *Cell,* 184**,** 4220-4236.e13.
702 LU, R., ZHAO, X., LI, J., NIU, P., YANG, B., WU, H., WANG, W., SONG, H., HUANG, B., ZHU, N.,
703 BI, Y., MA, X., ZHAN, F., WANG, L., HU, T., ZHOU, H., HU, Z., ZHOU, W., ZHAO, L.,
704 CHEN, J., MENG, Y., WANG, J., LIN, Y., YUAN, J., XIE, Z., MA, J., LIU, W. J., WANG, D.,

XU, W., HOLMES, E. C., GAO, G. F., WU, G., CHEN, W., SHI, W. & TAN, W. 2020. Genomic characterisation and epidemiology of 2019 novel coronavirus: implications for virus origins and receptor binding. *The Lancet,* 395**,** 565-574.

LU, T., WANG, Y. & GUO, T. 2022. Multi-omics in COVID-19: Seeing the unseen but overlooked in the clinic. *Cell Reports Medicine,* 3**,** 100580.

MANZINI, M. C., XIONG, L., SHAHEEN, R., TAMBUNAN, DIMIRA E., DI COSTANZO, S., MITISALIS, V., TISCHFIELD, DAVID J., CINQUINO, A., GHAZIUDDIN, M., CHRISTIAN, M., JIANG, Q., LAURENT, S., NANJIANI, ZOHAIR A., RASHEED, S., HILL, R. S., LIZARRAGA, SOFIA B., GLEASON, D., SABBAGH, D., SALIH, MUSTAFA A., ALKURAYA, FOWZAN S. & WALSH, CHRISTOPHER A. 2014. CC2D1A Regulates Human Intellectual and Social Function as well as NF-κB Signaling Homeostasis. *Cell Reports,* 8**,** 647-655.

MCCALLUM, M., CZUDNOCHOWSKI, N., ROSEN, L. E., ZEPEDA, S. K., BOWEN, J. E., WALLS, A. C., HAUSER, K., JOSHI, A., STEWART, C., DILLEN, J. R., POWELL, A. E., CROLL, T. I., NIX, J., VIRGIN, H. W., CORTI, D., SNELL, G. & VEESLER, D. 2022. Structural basis of SARS-CoV-2 Omicron immune evasion and receptor engagement. *Science,* 375**,** 864-868.

MILANINI-MONGIAT, J., POUYSSéGUR, J. & PAGèS, G. 2002. Identification of Two Sp1 Phosphorylation Sites for p42/p44 Mitogen-activated Protein Kinases: THEIR IMPLICATION IN VASCULAR ENDOTHELIAL GROWTH FACTOR GENE TRANSCRIPTION*. *Journal of Biological Chemistry,* 277**,** 20631-20639.

MONTEIL, V., KWON, H., PRADO, P., HAGELKRüYS, A., WIMMER, R. A., STAHL, M., LEOPOLDI, A., GARRETA, E., HURTADO DEL POZO, C., PROSPER, F., ROMERO, J. P.,

WIRNSBERGER, G., ZHANG, H., SLUTSKY, A. S., CONDER, R., MONTSERRAT, N., MIRAZIMI, A. & PENNINGER, J. M. 2020. Inhibition of SARS-CoV-2 Infections in Engineered Human Tissues Using Clinical-Grade Soluble Human ACE2. *Cell,* 181**,** 905-913.e7.

MUñOZ-FONTELA, C., DOWLING, W. E., FUNNELL, S. G. P., GSELL, P.-S., RIVEROS-BALTA, A. X., ALBRECHT, R. A., ANDERSEN, H., BARIC, R. S., CARROLL, M. W., CAVALERI, M., QIN, C., CROZIER, I., DALLMEIER, K., DE WAAL, L., DE WIT, E., DELANG, L., DOHM, E., DUPREX, W. P., FALZARANO, D., FINCH, C. L., FRIEMAN, M. B., GRAHAM, B. S., GRALINSKI, L. E., GUILFOYLE, K., HAAGMANS, B. L., HAMILTON, G. A., HARTMAN, A. L., HERFST, S., KAPTEIN, S. J. F., KLIMSTRA, W. B., KNEZEVIC, I., KRAUSE, P. R., KUHN, J. H., LE GRAND, R., LEWIS, M. G., LIU, W.-C., MAISONNASSE, P., MCELROY, A. K., MUNSTER, V., ORESHKOVA, N., RASMUSSEN, A. L., ROCHA-PEREIRA, J., ROCKX, B., RODRíGUEZ, E., ROGERS, T. F., SALGUERO, F. J., SCHOTSAERT, M., STITTELAAR, K. J., THIBAUT, H. J., TSENG, C.-T., VERGARA-ALERT, J., BEER, M., BRASEL, T., CHAN, J. F. W., GARCíA-SASTRE, A., NEYTS, J., PERLMAN, S., REED, D. S., RICHT, J. A., ROY, C. J., SEGALéS, J., VASAN, S. S., HENAO-RESTREPO, A. M. & BAROUCH, D. H. 2020. Animal models for COVID-19. *Nature,* 586**,** 509-515.

NADIM, M. K., FORNI, L. G., MEHTA, R. L., CONNOR, M. J., LIU, K. D., OSTERMANN, M., RIMMELé, T., ZARBOCK, A., BELL, S., BIHORAC, A., CANTALUPPI, V., HOSTE, E., HUSAIN-SYED, F., GERMAIN, M. J., GOLDSTEIN, S. L., GUPTA, S., JOANNIDIS, M., KASHANI, K., KOYNER, J. L., LEGRAND, M., LUMLERTGUL, N., MOHAN, S., PANNU, N., PENG, Z., PEREZ-FERNANDEZ, X. L., PICKKERS, P., PROWLE, J., REIS, T., SRISAWAT, N., TOLWANI, A., VIJAYAN, A., VILLA, G., YANG, L., RONCO, C. &

KELLUM, J. A. 2020. COVID-19-associated acute kidney injury: consensus report of the 25th Acute Disease Quality Initiative (ADQI) Workgroup. *Nature Reviews Nephrology,* 16**,** 747-764.

PAN, Y., DU, J., LIU, J., WU, H., GUI, F., ZHANG, N., DENG, X., SONG, G., LI, Y., LU, J., WU, X., ZHAN, S., JING, Z., WANG, J., YANG, Y., LIU, J., CHEN, Y., CHEN, Q., ZHANG, H., HU, H., DUAN, K., WANG, M., WANG, Q. & YANG, X. 2021. Screening of potent neutralizing antibodies against SARS-CoV-2 using convalescent patients-derived phage-display libraries. *Cell Discovery,* 7**,** 57.

QIAO, Y. Y., WANG, X. M., MANNAN, R., PITCHIAYA, S., ZHANG, Y. P., WOTRING, J. W., XIAO, L. B., ROBINSON, D. R., WU, Y. M., TIEN, J. C. Y., CAO, X. H., SIMKO, S. A., APEL, I. J., BAWA, P., KREGEL, S., NARAYANAN, S. P., RASKIND, G., ELLISON, S. J., PAROLIA, A., ZELENKA-WANG, S., MCMURRY, L., SU, F. Y., WANG, R., CHENG, Y. H., DELEKTA, A. D., MEI, Z. J., PRETTO, C. D., WANG, S. M., MEHRA, R., SEXTON, J. Z. & CHINNAIYAN, A. M. 2021. Targeting transcriptional regulation of SARS-CoV-2 entry factors ACE2 and TMPRSS2. *Proceedings of the National Academy of Sciences of the United States of America,* 118.

ROSENKE, K., HANSEN, F., SCHWARZ, B., FELDMANN, F., HADDOCK, E., ROSENKE, R., BARBIAN, K., MEADE-WHITE, K., OKUMURA, A., LEVENTHAL, S., HAWMAN, D. W., RICOTTA, E., BOSIO, C. M., MARTENS, C., SATURDAY, G., FELDMANN, H. & JARVIS, M. A. 2021. Orally delivered MK-4482 inhibits SARS-CoV-2 replication in the Syrian hamster model. *Nature Communications,* 12**,** 2295.

SAMUEL, R. M., MAJD, H., RICHTER, M. N., GHAZIZADEH, Z., ZEKAVAT, S. M., NAVICKAS, A., RAMIREZ, J. T., ASGHARIAN, H., SIMONEAU, C. R., BONSER, L. R., KOH, K. D.,

GARCIA-KNIGHT, M., TASSETTO, M., SUNSHINE, S., FARAHVASHI, S., KALANTARI, A., LIU, W., ANDINO, R., ZHAO, H., NATARAJAN, P., ERLE, D. J., OTT, M., GOODARZI, H. & FATTAHI, F. 2020. Androgen Signaling Regulates SARS-CoV-2 Receptor Levels and Is Associated with Severe COVID-19 Symptoms in Men. *Cell Stem Cell,* 27**,** 876-889.e12.

SCHLESINGER, N., FIRESTEIN, B. L. & BRUNETTI, L. 2020. Colchicine in COVID-19: an Old Drug, New Use. *Current Pharmacology Reports,* 6**,** 137-145.

SIA, S. F., YAN, L.-M., CHIN, A. W. H., FUNG, K., CHOY, K.-T., WONG, A. Y. L., KAEWPREEDEE, P., PERERA, R. A. P. M., POON, L. L. M., NICHOLLS, J. M., PEIRIS, M. & YEN, H.-L. 2020. Pathogenesis and transmission of SARS-CoV-2 in golden hamsters. *Nature,* 583**,** 834-838.

SLOBODNICK, A., SHAH, B., PILLINGER, M. H. & KRASNOKUTSKY, S. 2015. Colchicine: Old and New. *The American Journal of Medicine,* 128**,** 461-470.

SMITH, K. D. & AKILESH, S. 2021. Pathogenesis of coronavirus disease 2019-associated kidney injury. *Current Opinion in Nephrology and Hypertension,* 30.

SU, C.-H., WANG, C.-Y., LAN, K.-H., LI, C.-P., CHAO, Y., LIN, H.-C., LEE, S.-D. & LEE, W.-P. 2011. Akt phosphorylation at Thr308 and Ser473 is required for CHIP-mediated ubiquitination of the kinase. *Cellular Signalling,* 23**,** 1824-1830.

SUN, F., MU, C., KWOK, H. F., XU, J., WU, Y., LIU, W., SABATIER, J. M., ANNWEILER, C., LI, X., CAO, Z. & XIE, Y. 2021. Capivasertib restricts SARS-CoV-2 cellular entry: a potential clinical application for COVID-19. *International Journal of Biological Sciences,* 17**,** 2348-2355.

TAO, J., MA, Y.-C., YANG, Z.-S., ZOU, C.-G. & ZHANG, K.-Q. 2016. Octopamine connects nutrient cues to lipid metabolism upon nutrient deprivation. *Science Advances,* 2**,** e1501372.

VAN EIJK, L. E., BINKHORST, M., BOURGONJE, A. R., OFFRINGA, A. K., MULDER, D. J., BOS,

E. M., KOLUNDZIC, N., ABDULLE, A. E., VAN DER VOORT, P. H. J., OLDE RIKKERT, M. G. M., VAN DER HOEVEN, J. G., DEN DUNNEN, W. F. A., HILLEBRANDS, J.-L. & VAN GOOR, H. 2021. COVID-19: immunopathology, pathophysiological mechanisms, and treatment options. *The Journal of Pathology,* 254**,** 307-331.

VERDECCHIA, P., CAVALLINI, C., SPANEVELLO, A. & ANGELI, F. 2020. The pivotal link between ACE2 deficiency and SARS-CoV-2 infection. *European Journal of Internal Medicine,* 76**,** 14-20.

WEI, J., ALFAJARO, M. M., DEWEIRDT, P. C., HANNA, R. E., LU-CULLIGAN, W. J., CAI, W. L., STRINE, M. S., ZHANG, S.-M., GRAZIANO, V. R., SCHMITZ, C. O., CHEN, J. S., MANKOWSKI, M. C., FILLER, R. B., RAVINDRA, N. G., GASQUE, V., DE MIGUEL, F. J., PATIL, A., CHEN, H., OGUNTUYO, K. Y., ABRIOLA, L., SUROVTSEVA, Y. V., ORCHARD, R. C., LEE, B., LINDENBACH, B. D., POLITI, K., VAN DIJK, D., KADOCH, C., SIMON, M. D., YAN, Q., DOENCH, J. G. & WILEN, C. B. 2021. Genome-wide CRISPR Screens Reveal Host Factors Critical for SARS-CoV-2 Infection. *Cell,* 184**,** 76-91.e13.

WILHELM, A., WIDERA, M., GRIKSCHEIT, K., TOPTAN, T., SCHENK, B., PALLAS, C., METZLER, M., KOHMER, N., HOEHL, S., MARSCHALEK, R., HERRMANN, E., HELFRITZ, F. A., WOLF, T., GOETSCH, U. & CIESEK, S. 2022. Limited neutralisation of the SARS-CoV-2 Omicron subvariants BA.1 and BA.2 by convalescent and vaccine serum and monoclonal antibodies. *eBioMedicine,* 82**,** 104158.

WU, F., ZHAO, S., YU, B., CHEN, Y.-M., WANG, W., SONG, Z.-G., HU, Y., TAO, Z.-W., TIAN, J.-H., PEI, Y.-Y., YUAN, M.-L., ZHANG, Y.-L., DAI, F.-H., LIU, Y., WANG, Q.-M., ZHENG, J.-J., XU, L., HOLMES, E. C. & ZHANG, Y.-Z. 2020. A new coronavirus associated with human

815 respiratory disease in China. *Nature,* 579**,** 265-269.

816 WYSOCKI, J., YE, M., HASSLER, L., GUPTA, A. K., WANG, Y., NICOLEASCU, V., RANDALL, G.,
817 WERTHEIM, J. A. & BATLLE, D. 2021. A Novel Soluble ACE2 Variant with Prolonged
818 Duration of Action Neutralizes SARS-CoV-2 Infection in Human Kidney Organoids. *Journal*
819 *of the American Society of Nephrology,* 32**,** 795.

820 XU, G., LI, Y., ZHANG, S., PENG, H., WANG, Y., LI, D., JIN, T., HE, Z., TONG, Y., QI, C., WU, G.,
821 DONG, K., GOU, J., LIU, Y., XIAO, T., QU, J., LI, L., LIU, L., ZHAO, P., ZHANG, Z. &
822 YUAN, J. 2021a. SARS-CoV-2 promotes RIPK1 activation to facilitate viral propagation. *Cell*
823 *Research,* 31**,** 1230-1243.

824 XU, Y., ZHANG, S., LIAO, X., LI, M., CHEN, S., LI, X., WU, X., YANG, M., TANG, M., HU, Y., LI,
825 Z., YU, R., HUANG, M., SONG, L. & LI, J. 2021b. Circular RNA circIKBKB promotes breast
826 cancer bone metastasis through sustaining NF-κB/bone remodeling factors signaling. *Molecular*
827 *Cancer,* 20**,** 98.

828 YAN, R., ZHANG, Y., LI, Y., XIA, L., GUO, Y. & ZHOU, Q. 2020. Structural basis for the recognition
829 of SARS-CoV-2 by full-length human ACE2. *Science,* 367**,** 1444-1448.

830 YIN, W., XU, Y., XU, P., CAO, X., WU, C., GU, C., HE, X., WANG, X., HUANG, S., YUAN, Q., WU,
831 K., HU, W., HUANG, Z., LIU, J., WANG, Z., JIA, F., XIA, K., LIU, P., WANG, X., SONG, B.,
832 ZHENG, J., JIANG, H., CHENG, X., JIANG, Y., DENG, S.-J. & XU, H. E. 2022. Structures of
833 the Omicron spike trimer with ACE2 and an anti-Omicron antibody. *Science,* 375**,** 1048-1053.

834 ZHAO, J., YE, W., WU, J., LIU, L., YANG, L., GAO, L., CHEN, B., ZHANG, F., YANG, H. & LI, Y.
835 2015. Sp1-CD147 positive feedback loop promotes the invasion ability of ovarian cancer.
836 *Oncology Reports,* 34**,** 67-76.

837 ZHOU, Y., WANG, M., LI, Y., WANG, P., ZHAO, P., YANG, Z., WANG, S., ZHANG, L., LI, Z., JIA,
838 K., ZHONG, C., LI, N., YU, Y. & HOU, J. 2021. SARS-CoV-2 Spike protein enhances ACE2
839 expression via facilitating Interferon effects in bronchial epithelium. *Immunology Letters,* 237**,**
840 33-41.
841 ZHUANG, M.-W., CHENG, Y., ZHANG, J., JIANG, X.-M., WANG, L., DENG, J. & WANG, P.-H. 2020.
842 Increasing host cellular receptor—angiotensin-converting enzyme 2 expression by coronavirus
843 may facilitate 2019-nCoV (or SARS-CoV-2) infection. *Journal of Medical Virology,* 92**,** 2693-
844 2701.
845 ZIEGLER, C. G. K., ALLON, S. J., NYQUIST, S. K., MBANO, I. M., MIAO, V. N., TZOUANAS, C.
846 N., CAO, Y., YOUSIF, A. S., BALS, J., HAUSER, B. M., FELDMAN, J., MUUS, C.,
847 WADSWORTH, M. H., KAZER, S. W., HUGHES, T. K., DORAN, B., GATTER, G. J.,
848 VUKOVIC, M., TALIAFERRO, F., MEAD, B. E., GUO, Z., WANG, J. P., GRAS, D.,
849 PLAISANT, M., ANSARI, M., ANGELIDIS, I., ADLER, H., SUCRE, J. M. S., TAYLOR, C.
850 J., LIN, B., WAGHRAY, A., MITSIALIS, V., DWYER, D. F., BUCHHEIT, K. M., BOYCE, J.
851 A., BARRETT, N. A., LAIDLAW, T. M., CARROLL, S. L., COLONNA, L., TKACHEV, V.,
852 PETERSON, C. W., YU, A., ZHENG, H. B., GIDEON, H. P., WINCHELL, C. G., LIN, P. L.,
853 BINGLE, C. D., SNAPPER, S. B., KROPSKI, J. A., THEIS, F. J., SCHILLER, H. B.,
854 ZARAGOSI, L.-E., BARBRY, P., LESLIE, A., KIEM, H.-P., FLYNN, J. L., FORTUNE, S. M.,
855 BERGER, B., FINBERG, R. W., KEAN, L. S., GARBER, M., SCHMIDT, A. G., LINGWOOD,
856 D., SHALEK, A. K., ORDOVAS-MONTANES, J., BANOVICH, N., BARBRY, P., BRAZMA,
857 A., DESAI, T., DUONG, T. E., EICKELBERG, O., FALK, C., FARZAN, M., GLASS, I.,
858 HANIFFA, M., HORVATH, P., HUNG, D., KAMINSKI, N., KRASNOW, M., KROPSKI, J. A.,

KUHNEMUND, M., LAFYATIS, R., LEE, H., LEROY, S., LINNARSON, S., LUNDEBERG, J., MEYER, K., MISHARIN, A., NAWIJN, M., NIKOLIC, M. Z., ORDOVAS-MONTANES, J., PE'ER, D., POWELL, J., QUAKE, S., RAJAGOPAL, J., TATA, P. R., RAWLINS, E. L., REGEV, A., REYFMAN, P. A., ROJAS, M., et al. 2020. SARS-CoV-2 Receptor ACE2 Is an Interferon-Stimulated Gene in Human Airway Epithelial Cells and Is Detected in Specific Cell Subsets across Tissues. *Cell,* 181**,** 1016-1035.e19.

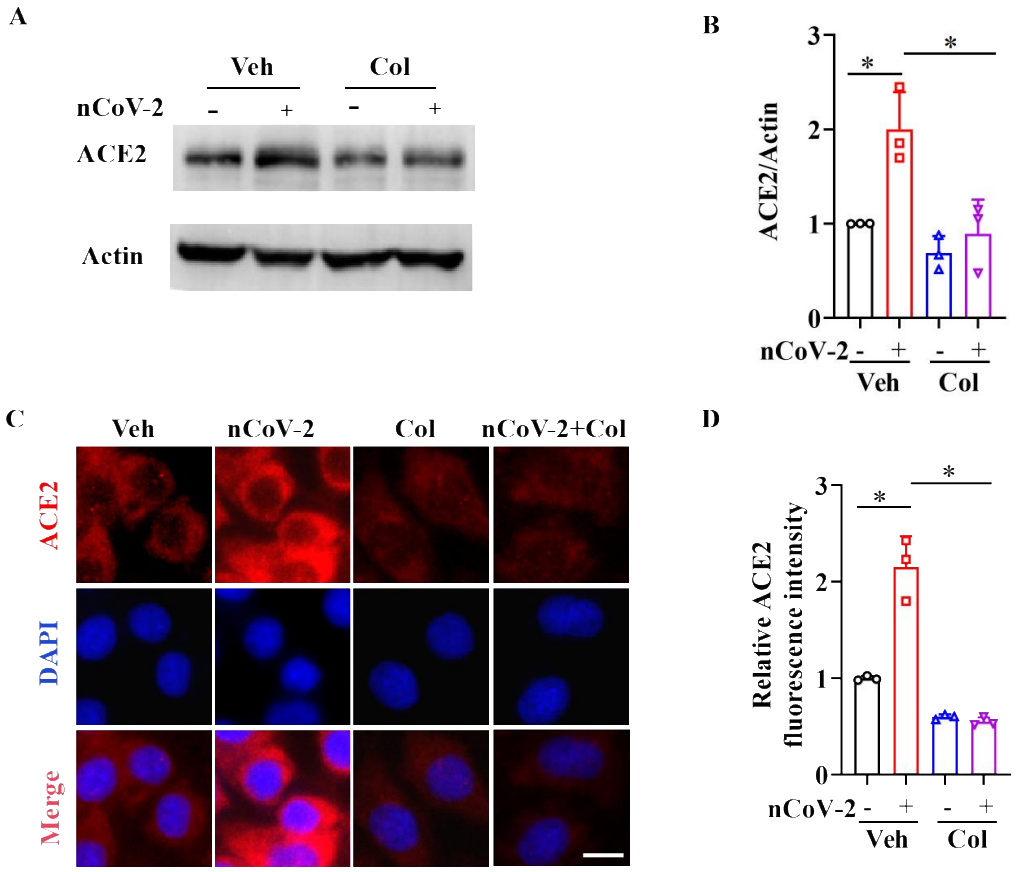

881

882 **Figure 1. SARS-CoV-2 infection up-regulates ACE2 expression, which is suppressed by**

883 **colchicine.** (**A** and **B**) SARS-CoV-2 infection up-regulated the protein levels of ACE2.

884 Colchicine (20 nM) significantly reduced the protein levels of ACE2 in HPAEpiC cells. The

885 blot is typical of three independent experiments (**A**). Quantification of the ratio of ACE2 to

886 Actin (**B**). These results are means ± SD of three independent experiments. *P < 0.05 (unpaired

887 Student's t test). (**C**) Representative images of immunofluorescence staining for ACE2. Scale

888 bar: 10 μm. (**D**) Quantification of ACE2 fluorescence intensity. These results are means ± SD

889 of three independent experiments. *P < 0.05 (unpaired Student's t test). Veh, Vehicle. Col,

890 Colchicine. nCoV-2, SARS-CoV-2.

891 **Figure 1-source data 1**

892 Original uncropped Western blot images in Figure 1A (anti-ACE2 and anti-Actin).

Figure 1-source data 2

PDF containing Figure 1A and original scans of the relevant Western blot analysis (anti-ACE2 and anti-Actin) with highlighted bands and sample labels.

Figure 1-source data 3

Original file for quantification the ratio of ACE2 to Actin in Figure 1B (anti-ACE2 and anti-Actin).

Figure 1-source data 4

Original file for quantification of ACE2 fluorescence intensity in Figure 1D.

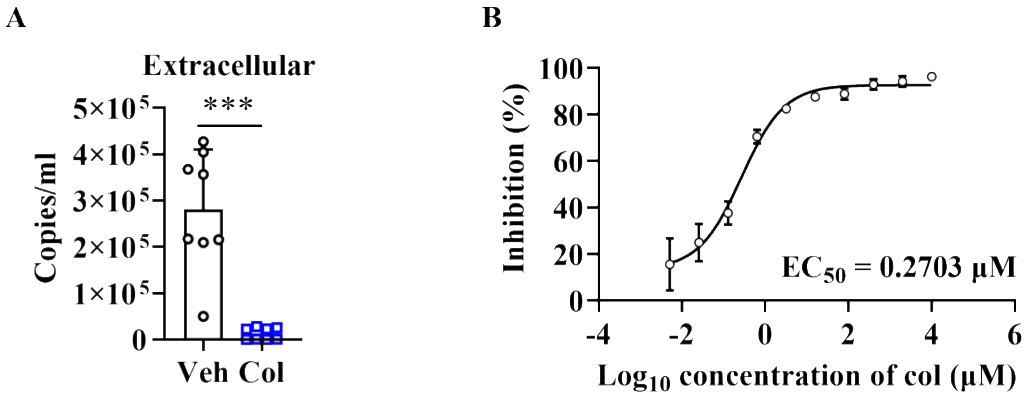

Figure 1-figure supplement 1. Colchicine blocks SARS-CoV-2 replication. (**A**) Colchicine (20 nM) inhibited SARS-CoV-2 replication in HPAEpiC cells. Cell culture supernatants were collected for viral load determination (n=8 each group). Error bars show means ± SD. ***P < 0.001 (unpaired Student's t test). (**B**) Dose-response analysis of HPAEpiC cells treated with colchicine at the indicated concentrations and infected with SARS-CoV-2 (MOI = 1) for 48 hours.

Figure 1-figure supplement 1-source data 1

Original file for determination of viral load in Figure 1-figure supplement 1A.

Figure 1-figure supplement 1-source data 2

Original file for dose-response analysis in Figure 1-figure supplement 1B.

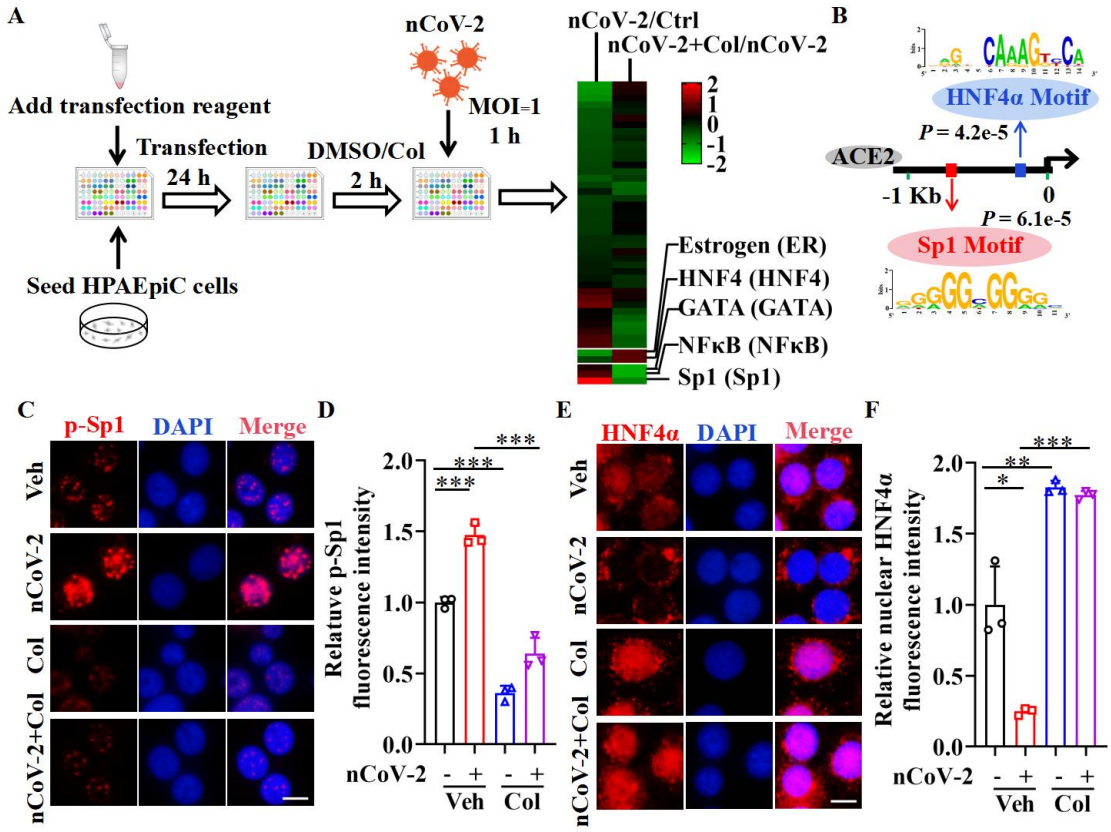

933

934 **Figure 2. The activation of Sp1 and inactivation of HNF4α are mediated by SARS-CoV-2.**

935 (**A**) Assays for the signaling pathways in response to SARS-CoV-2 infection and colchicine

936 treatment (20 nM) using cignal finder 45-pathway reporter array. (**B**) The Sp1 and HNF4α

937 binding elements in 1.5 kb upstream of the transcription start sites (TSS) of ACE2 gene

938 identified by the MEME program. (**C and D**) SARS-CoV-2 significantly increased the

939 phosphorylation of Sp1 (p-Sp1) in HPAEpiC cells, which was suppressed by treating with

940 colchicine (20 nM). Representative images of immunofluorescence staining for p-Sp1 (**C**).

941 Scale bar: 10 μm. Quantification of p-Sp1 fluorescence intensity (**D**). These results are means

942 ± SD of three independent experiments. ***$P < 0.001$ (unpaired Student's t test). (**E and F**)

943 SARS-CoV-2 induced cytoplasmic translocation of HNF4α, whereas colchicine (20 nM)

944 promoted its nuclear accumulation in HPAEpiC cells. Representative images of

945 immunofluorescence staining for HNF4α (**E**). Scale bar: 10 μm. Quantification of HNF4α

946 fluorescence intensity (**F**). These results are means ± SD of three independent experiments. *P

947 < 0.05, **$P < 0.01$, ***$P < 0.001$ (unpaired Student's t test). Veh, Vehicle. Col, Colchicine.

948 nCoV-2, SARS-CoV-2.

949 **Figure 2-source data 1**

950 Original file for quantification of p-Sp1 fluorescence intensity in Figure 2D.

951 **Figure 2-source data 2**

952 Original file for quantification of HNF4α fluorescence intensity in Figure 2F.

953

954

955

956

957

958

959

960

961

962

963

964

965

966

967

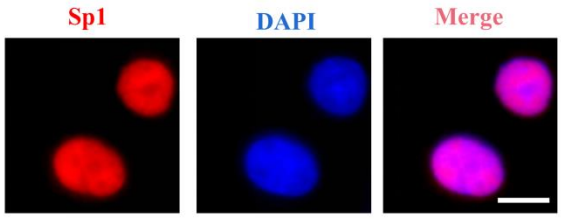

968

969 **Figure 2-figure supplement 1. Sp1 is mainly located in nucleus of HPAEpiC cells.**

970

971

972

973

974

975

976

977

978

979

980

981

982

983

984

985

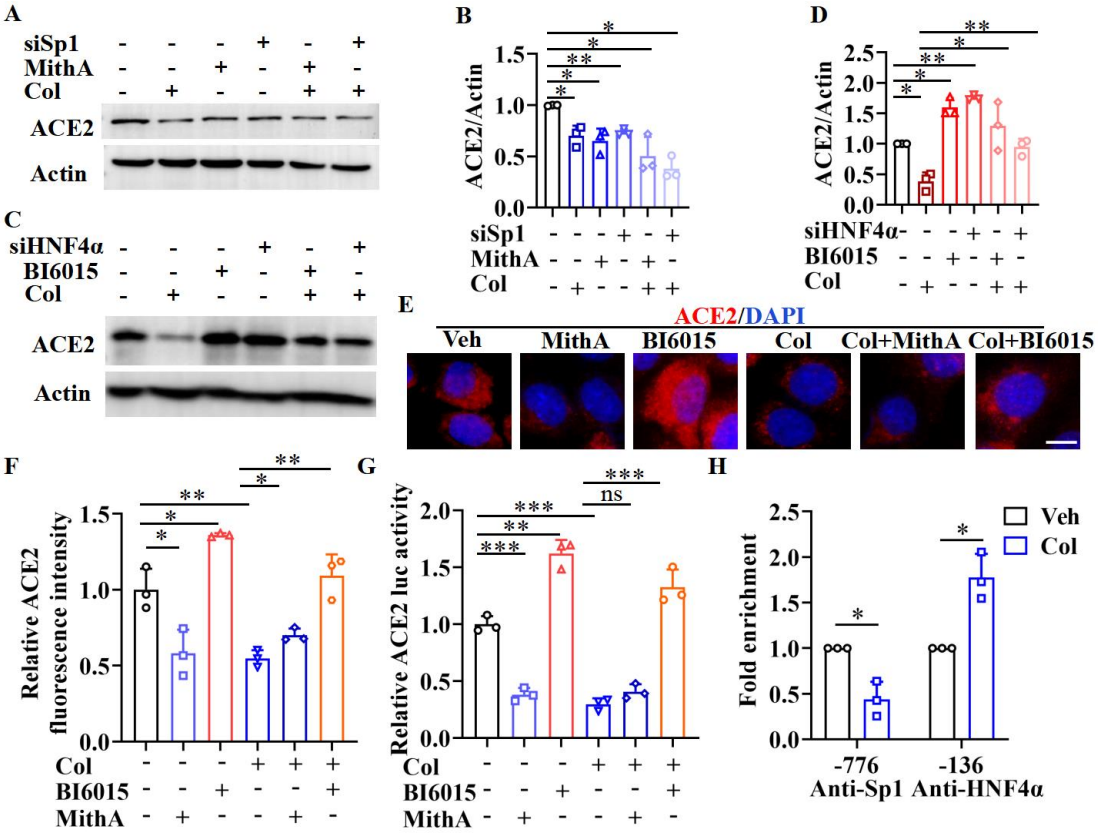

Figure 3. Sp1 and HNF4α act in an opposite way on the regulation of ACE2 expression.

(**A and B**) Supplementation with colchicine (20 nM), MithA (100 nM), colchicine + MithA, siSp1, or siSp1 + colchicine significantly suppressed the levels of ACE2 in HPAEpiC cells. The blot is typical of three independent experiments (**A**). Quantification the ratio of ACE2 to Actin (**B**). These results are means ± SD of three independent experiments. *$P < 0.05$, **$P < 0.01$ (unpaired Student's t test). (**C and D**) Supplementation with colchicine (20 nM) significantly suppressed the levels of ACE2 in HPAEpiC cells, which was reversed by treating with BI6015 (20 μM) or siHNF4α. The blot is typical of three independent experiments (**C**). Quantification the ratio of ACE2 to Actin (**D**). These results are means ± SD of three independent experiments. *$P < 0.05$, **$P < 0.01$ (unpaired Student's t test). (**E and F**) Representative images of immunofluorescence staining for ACE2 in HPAEpiC cells (**E**). HPAEpiC cells were treated with MithA (100 nM), BI6015 (20 μM), colchicine (20 nM), colchicine + MithA, or colchicine

+ BI6015. Scale bar: 10 μm. Quantification of ACE2 fluorescence intensity (**F**). These results are means ± SD of three independent experiments. *$P < 0.05$, **$P < 0.01$ (unpaired Student's t test). (**G**) Luciferase activity analysis of ACE2 promoter in HPAEpiC cells. These results are means ± SD of three independent experiments. **$P < 0.01$, ***$P < 0.001$, ns, not significant (unpaired Student's t test). (**H**) The putative Sp1 and HNF4α binding sites in the promoter regions of ACE2 were detected by ChIP-qPCR with anti-Sp1 and anti-HNF4α antibodies. These results are means ± SD of three independent experiments. *$P < 0.05$. Veh, Vehicle. Col, Colchicine.

Figure 3-source data 1

Original uncropped Western blot images in Figure 3A (anti-ACE2 and anti-Actin).

Figure 3-source data 2

Original uncropped Western blot images in Figure 3C (anti-ACE2 and anti-Actin).

Figure 3-source data 3

PDF containing Figure 3A and 3C and original scans of the relevant Western blot analysis (anti-ACE2 and anti-Actin) with highlighted bands and sample labels.

Figure 3-source data 4

Original file for quantification the ratio of ACE2 to Actin in Figure 3B and 3D (anti-ACE2 and anti-Actin).

Figure 3-source data 5

Original file for quantification of ACE2 fluorescence intensity in Figure 3F.

Figure 3-source data 6

Original file for luciferase activity analysis in Figure 3G.

Figure 3-source data 7

Original file for ChIP analysis in Figure 3H.

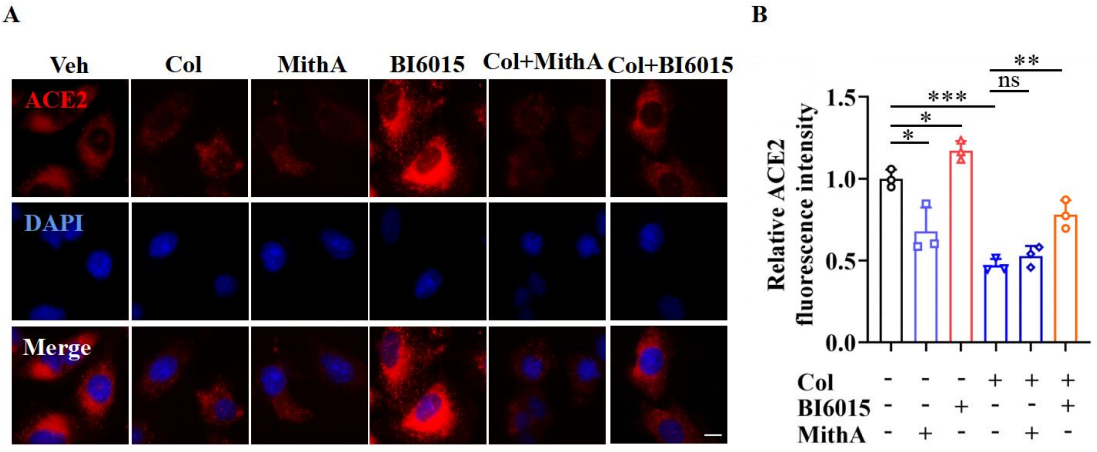

Figure 3-figure supplement 1. Immunofluorescence analysis of the expression and localization of ACE2 in A549 cells. (A) Representative images of immunofluorescence staining for ACE2 in A549 cells. A549 cells were treated with MithA, BI6015, colchicine, colchicine + MithA, or colchicine + BI6015. Scale bar: 10 μm. (**B**) Quantification of ACE2 fluorescence intensity. These results are means ± SD of three independent experiments. **P* < 0.05, ***P* < 0.01, ****P* < 0.001, ns, not significant (unpaired Student's t test). Veh, Vehicle. Col, Colchicine.

Figure 3-figure supplement 1-source data 1

Original file for quantification of ACE2 fluorescence intensity in Figure 3-figure supplement 1B.

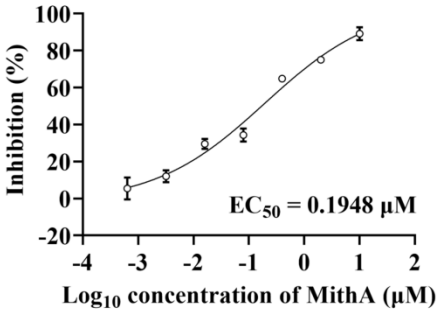

Figure 3-figure supplement 2. MithA inhibited SARS-CoV-2 replication in a dose-dependent manner. Dose-response analysis of HPAEpiC cells treated with the indicated concentrations of MithA and infected with SARS-CoV-2 (MOI = 1) for 48 hours. EC50 was achieved by plaque reduction assay and plotted using logistic non-linear regression model.

Figure 3-figure supplement 2-source data 1

Original file for dose-response analysis in Figure 3-figure supplement 2.

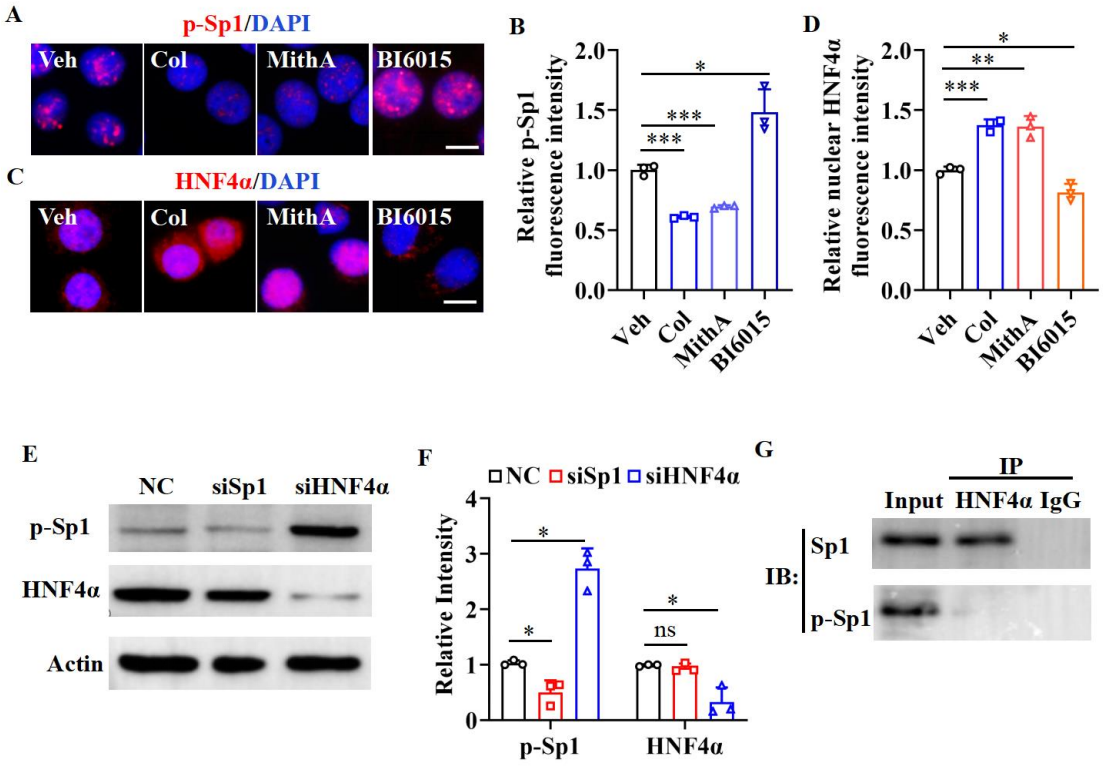

1072

1073 **Figure 4. Sp1 and HNF4α antagonize each other via protein-protein interaction.** (**A and**

1074 **B**) Supplementation with colchicine (20 nM) and MithA (100 nM) significantly suppressed the

1075 phosphorylation of Sp1 (p-Sp1) in HPAEpiC cells, which was reversed by treating with BI6015

1076 (20 μM). Representative images of immunofluorescence staining for p-Sp1 (**A**). Scale bar: 10

1077 μm. Quantification of p-Sp1 fluorescence intensity (**B**). These results are means ± SD of three

1078 independent experiments. *$P < 0.05$, ***$P < 0.001$ (unpaired Student's t test). (**C and D**)

1079 Supplementation with colchicine (20 nM) and MithA (100 nM) promoted nuclear accumulation

1080 of HNF4α in HPAEpiC cells, which was inhibited by treating with BI6015 (20 μM).

1081 Representative images of immunofluorescence staining for HNF4α (**C**). Scale bar: 10 μm.

1082 Quantification of HNF4α fluorescence intensity (**D**). These results are means ± SD of three

1083 independent experiments. *$P < 0.05$, **$P < 0.01$, ***$P < 0.001$ (unpaired Student's t test). (**E**

1084 **and F**) The phosphorylation levels of Sp1 and the total protein levels of HNF4α were measured

in HPAEpiC cells by Western blotting. The blot is typical of three independent experiments (**E**). Quantification of the ratio of p-Sp1 or HNF4α to Actin (**F**). These results are means ± SD of three independent experiments. **P* < 0.05, ns, not significant (unpaired Student's t test). (**G**) The interaction between Sp1 and HNF4α measured by Co-immunoprecipitation assay (co-IP) in HPAEpiC cells. NC, Negative control. Veh, Vehicle. Col, Colchicine.

Figure 4-source data 1

Original file for quantification of p-Sp1 fluorescence intensity in Figure 4B.

Figure 4-source data 2

Original file for quantification of HNF4α fluorescence intensity in Figure 4D.

Figure 4-source data 3

Original uncropped Western blot images in Figure 4E (anti-p-Sp1, anti-HNF4α and anti-Actin).

Figure 4-source data 4

PDF containing Figure 4E and 4G and original scans of the relevant Western blot analysis (anti-p-Sp1, anti-HNF4α and anti-Actin) with highlighted bands and sample labels.

Figure 4-source data 5

Original file for quantification the ratio of p-Sp1 and HNF4α to Actin in Figure 4F (anti-p-Sp1, anti-HNF4α and anti-Actin).

Figure 4-source data 6

Original uncropped Western blot images in Figure 4G.

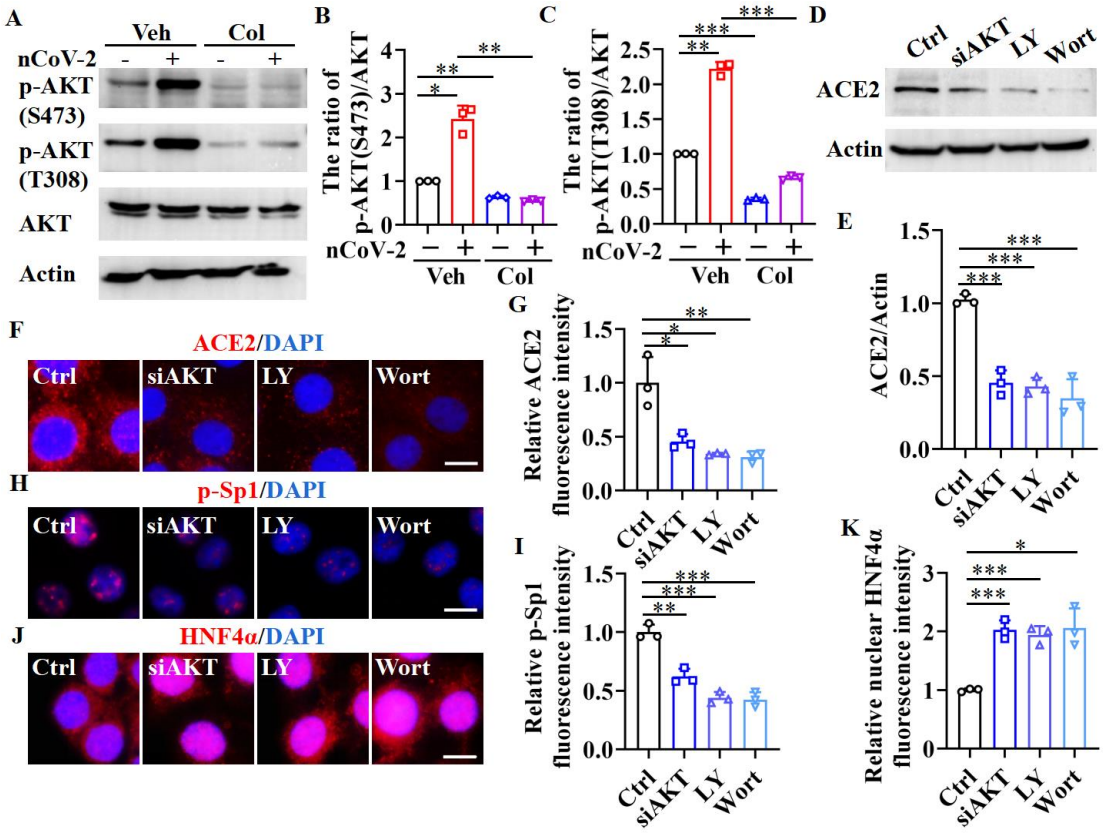

Figure 5. Sp1 and HNF4α are the downstream of PI3K/AKT signaling pathway. (**A-C**) The phosphorylation levels of AKT (S473 and T308) were measured in HPAEpiC cells by Western blotting. The blot is typical of three independent experiments (**A**). Quantification of the ratio of p-AKT (S473) (**B**) or p-AKT (T308) (**C**) to Actin. These results are means ± SD of three independent experiments. **P* < 0.05, ***P* < 0.01, ****P* < 0.001 (unpaired Student's t test). (**D-G**) Supplementation with LY294002 (30 μM) and wortmannin (50 nM), or siAKT significantly suppressed the levels of ACE2 in HPAEpiC cells. The blot is typical of three independent experiments (**D**). Quantification of the ratio of ACE2 to Actin (**E**). These results are means ± SD of three independent experiments. ****P* < 0.001 (unpaired Student's t test). Representative images of immunofluorescence staining for ACE2 (**F**). Scale bar: 10 μm. Quantification of ACE2 fluorescence intensity (**G**). These results are means ± SD of three independent experiments. **P* < 0.05, ***P* < 0.01 (unpaired Student's t test). (**H and I**)

Supplementation with LY294002 (30 μM) and wortmannin (50 nM), or siAKT significantly suppressed the phosphorylation of Sp1 (p-Sp1) in HPAEpiC cells. Representative images of immunofluorescence staining for p-Sp1 (**H**). Scale bar: 10 μm. Quantification of p-Sp1 fluorescence intensity (**I**). These results are means ± SD of three independent experiments. ** $P < 0.01$, *** $P < 0.001$ (unpaired Student's t test). (**J and K**) Supplementation with LY294002 (30 μM) and wortmannin (50 nM), or siAKT promoted nuclear accumulation HNF4α in HPAEpiC cells. Representative images of immunofluorescence staining for HNF4α (**J**). Scale bar: 10 μm. Quantification of HNF4α fluorescence intensity (**K**). These results are means ± SD of three independent experiments. * $P < 0.05$, *** $P < 0.001$ (unpaired Student's t test). Ctrl, Control. Veh, Vehicle. Col, Colchicine. LY, LY294002. Wort, wortmannin. nCoV-2, SARS-CoV-2.

Figure 5-source data 1

Original uncropped Western blot images in Figure 5A (anti-p-AKT (S473), anti-p-AKT (T308) and anti-Actin).

Figure 5-source data 2

PDF containing Figure 5A and 5D and original scans of the relevant Western blot analysis with highlighted bands and sample labels.

Figure 5-source data 3

Original file for quantification the ratio of p-AKT to AKT in Figure 5B and 5C.

Figure 5-source data 4

Original uncropped Western blot images in Figure 5D (anti-ACE2 and anti-Actin).

Figure 5-source data 5

Original file for quantification the ratio of ACE2 to Actin in Figure 5E.

Figure 5-source data 6

Original files for quantification of ACE2, p-Sp1 and HNF4α fluorescence intensity in Figure 5G, 5I and 5K.

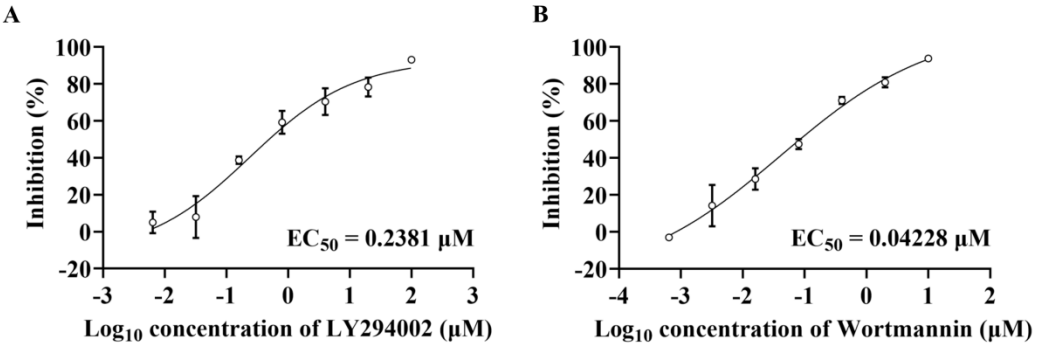

Figure 5-figure supplement 1. PI3K inhibitors inhibit SARS-CoV-2 replication in a dose-dependent manner. (**A and B**) Dose-response analysis of HPAEpiC cells treated with the indicated concentrations of PI3K/AKT inhibitors LY294002 (**A**) or wortmannin (**B**) and infected with SARS-CoV-2 (MOI = 1) for 48 hours. EC50 was achieved by plaque reduction assay and plotted using logistic non-linear regression model.

Figure 5-figure supplement 1-source data 1

Original file for dose-response analysis in Figure 5-figure supplement 1A and 1B.

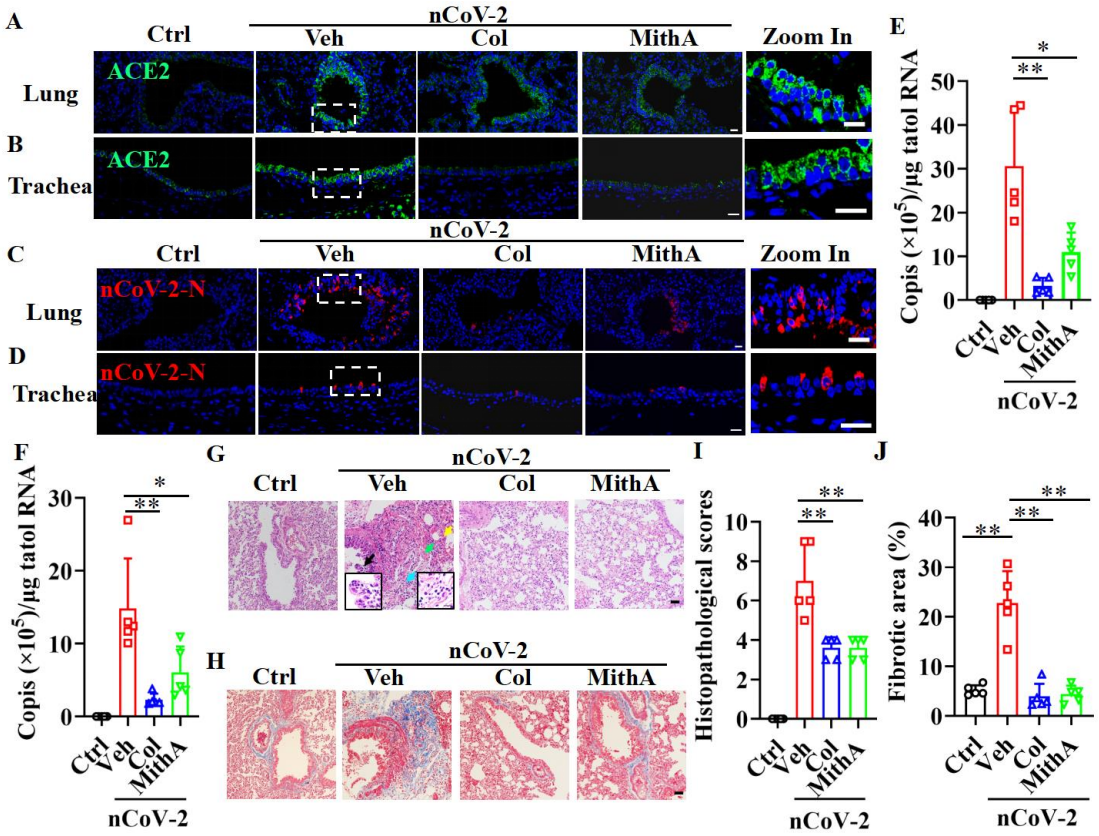

Figure 6. Inhibition of Sp1 inhibits the replication of SARS-CoV-2 and reduces lung pathology in Syrian hamsters. (**A and B**) Treatment of either colchicine or MithA inhibited the expression of ACE2 in the lung and trachea of hamsters infected with SARS-CoV-2. Representative images of immunofluorescence staining of ACE2 in the lung (**A**) and trachea (**B**) of hamsters. The parts on the right side are high-power images. Scale bar: 20 μm. (**C-F**) Treatment of either colchicine or MithA inhibited the replication of SARS-CoV-2 in the lung and trachea of hamsters. Representative images of immunofluorescence staining of SARS-CoV-2-N in the lung (**C**) and trachea (**D**) of hamsters. The parts on the right side are high-power images. Scale bar: 20 μm. Viral loads of SARS-CoV-2 were measured in the lung (**E**) and trachea (**F**) of hamsters by qPCR (n = 5 each group). Error bars show means ± SD. **P* < 0.05, ***P* < 0.01 (unpaired Student's t test). (**G-J**) Supplementation with either colchicine or MithA attenuated histopathological damage in the lung of hamsters infected with SARS-CoV-

2. Representative images of haematoxylin and eosin (HE) staining in lung of hamsters infected with SARS-CoV-2 at 3 dpi (**G**). Bronchial epithelial cell necrosis and pyknosis (black arrow), edema, loose arrangement of muscle fibers, and massive lymphocyte infiltration (blue arrow), extensive hemorrhage (green arrow), and alveolar wall thickening (yellow arrow). The parts on the lower side are high-power images of black arrow and blue arrow, respectively. Scale bar: 40 μm. Representative images of masson staining in lung of hamsters infected with SARS-CoV-2 at 3 dpi (**H**). Scale bar: 40 μm. Summary of lung lesion scoring in different groups at 3 dpi (n=5 each group) (**I**). Error bars show means ± SD. *P < 0.05 (unpaired Student's t test). Quantitative analysis of fibrotic area in lung tissues (**J**). Error bars show means ± SD. **P < 0.01 (unpaired Student's t test). Ctrl, Control. Veh, Vehicle. Col, Colchicine. nCoV-2, SARS-CoV-2.

Figure 6-source data 1

Original file for determination of viral load in Figure 6E.

Figure 6-source data 2

Original file for determination of viral load in Figure 6F.

Figure 6-source data 3

Original file for lesion scores in Figure 6I.

Figure 6-source data 4

Original file for quantitative analysis of fibrotic area in Figure 6J.

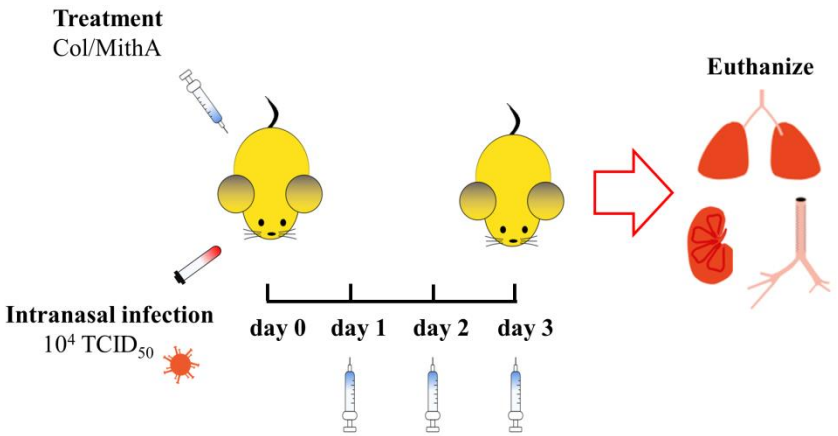

Figure 6-figure supplement 1. A schematic presentation of the experiment design for SARS-CoV-2 infection in Syrian hamsters.

On day 0 of SARS-CoV-2 infection in Syrian hamsters, colchicine and MithA were injected intraperitoneally, respectively, at a dose of 0.2 mg/kg/day. According to different groups, the drug was injected up to the 3th day after infection. The uninfected and placebo groups were given the same dose of vehicle daily. Five animals of each group were euthanized at 3 days post infection.

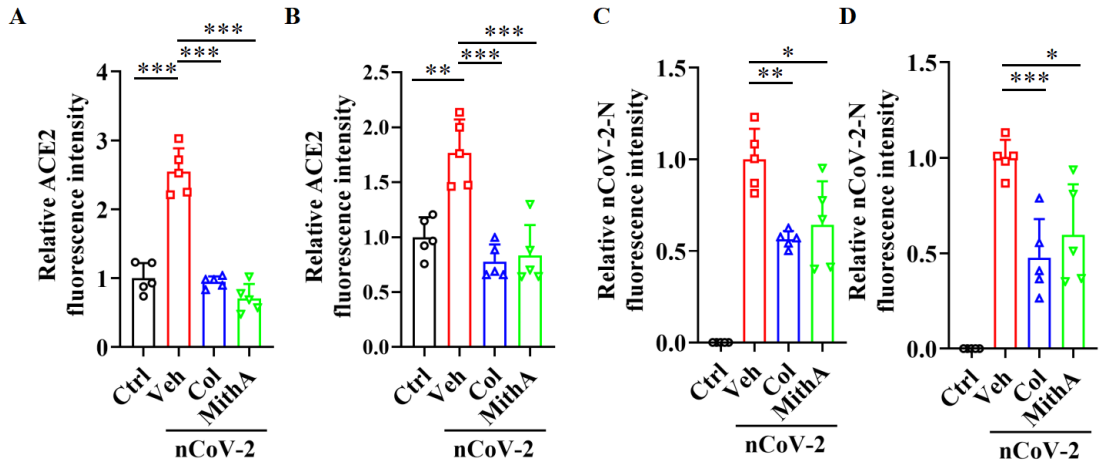

Figure 6-figure supplement 2. Either colchicine or MithA blocks the replication of SARS-CoV-2 by inhibiting the expression of ACE2 in both of the lung and trachea of hamsters. (**A and B**) Quantification of ACE2 fluorescence intensity in both of the lung (**A**) and trachea (**B**) of hamsters. Error bars show means ± SD. $^{**}P < 0.01$, $^{***}P < 0.001$ (Unpaired Student' s t test). (**C and D**) Quantification of SARS-CoV-2-N fluorescence intensity in both of the lung (**C**) and trachea (**D**) of hamsters. Error bars show means ± SD. $^{*}P < 0.05$, $^{**}P < 0.01$, $^{***}P < 0.001$ (Unpaired Student' s t test). Ctrl, Control. Veh, Vehicle. Col, Colchicine. nCoV-2, SARS-CoV-2.

Figure 6-figure supplement 2-source data 1

Original file for quantification of ACE2 fluorescence intensity in Figure 6-figure supplement 2A and 2B.

Figure 6-figure supplement 2-source data 2

Original file for quantification of SARS-CoV-2-N fluorescence intensity in Figure 6-figure supplement 2C and 2D.

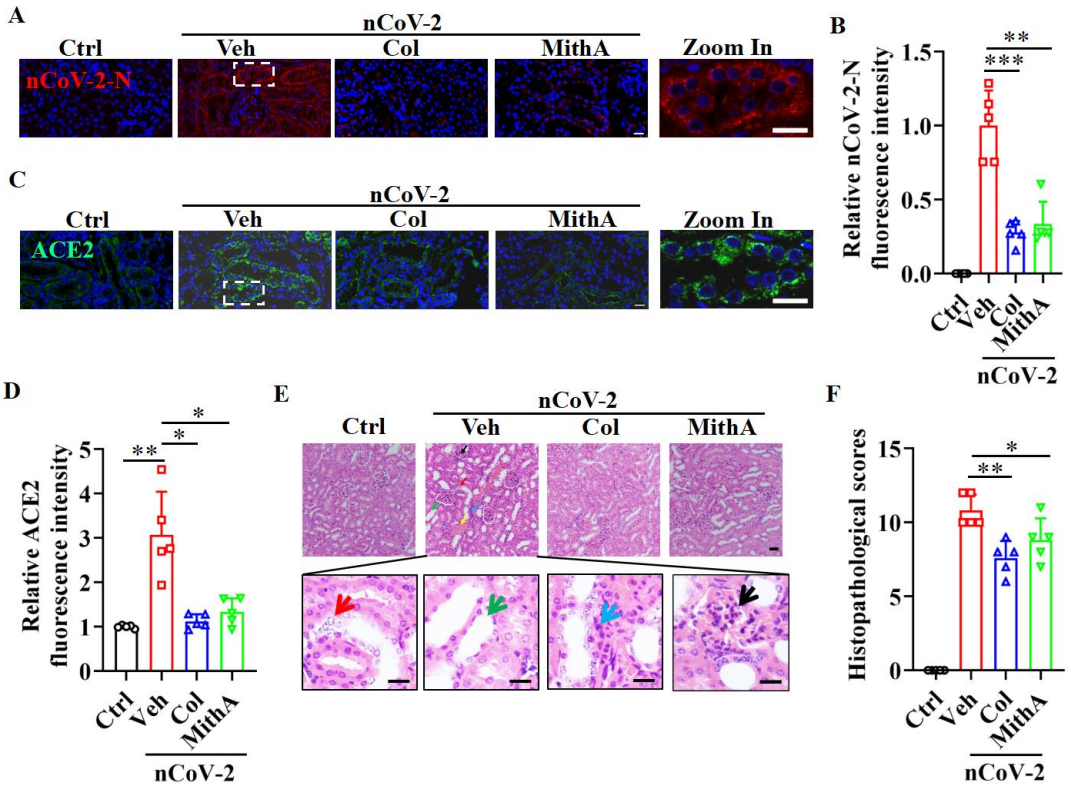

1249

1250 **Figure 7. Inhibition of Sp1 inhibits the replication of SARS-CoV-2 and reduces kidney**

1251 **pathology in Syrian hamsters.** (**A and B**) Treatment of either colchicine or MithA inhibited

1252 the replication of SARS-CoV-2 in the kidney of hamsters. Representative images of

1253 immunofluorescence staining of SARS-CoV-2-N in the kidney of hamsters (**A**). The parts on

1254 the right side are high-power images. Scale bar: 20 μm. Quantification of SARS-CoV-2-N

1255 fluorescence intensity in the kidney of hamsters (**B**). Error bars show means ± SD. $^{**}P < 0.01$,

1256 $^{***}P < 0.001$ (Unpaired Student's t test). (**C and D**) Treatment of either colchicine or MithA

1257 inhibited the expression of ACE2 in the kidney of hamsters infected with SARS-CoV-2.

1258 Representative images of immunofluorescence staining of ACE2 in the kidney of hamsters (**C**).

1259 The parts on the right side are high-power images. Scale bar: 20 μm. Quantification of ACE2

1260 fluorescence intensity in the kidney of hamsters (**D**). Error bars show means ± SD. $^{*}P < 0.05$,

1261 $^{**}P < 0.01$ (Unpaired Student's t test). (**E and F**) Supplementation with either colchicine or

MithA attenuated histopathological damage in the kidney of hamsters infected with SARS-CoV-2. Representative images of haematoxylin and eosin (HE) staining in the kidney of hamsters infected with SARS-CoV-2 at 3 dpi (**E**). Histopathology of kidney showed renal interstitial vascular congestion (black arrow), renal tubular epithelial cell nuclear pyknosis (red arrow), brush border disappearance (green arrow), renal interstitial inflammatory cell infiltration (blue arrow), and lomerular atrophy (yellow arrow). The parts on the lower side are high-power images of red arrow, green arrow, and blue arrow, respectively. Scale bar: 40 μm. Summary of kidney lesion scoring in different groups at 3 dpi (n=5 each group) (**F**). Error bars show means ± SD. *$P < 0.05$, **$P < 0.01$ (Unpaired Student’ s t test). Ctrl, Control. Veh, Vehicle. Col, Colchicine. nCoV-2, SARS-CoV-2.

Figure 7-source data 1

Original file for quantification of SARS-CoV-2-N fluorescence intensity in Figure 7B.

Figure 7-source data 2

Original file for quantification of ACE2 fluorescence intensity in Figure 7D.

Figure 7-source data 3

Original file for lesion scores in Figure 7F.